Fermi National Accelerator Laboratory

FERMILAB-Conf-91/200

Hyperons: Insights into Baryon Structures

J. Lach

Fermi National Accelerator Laboratory
P.O. Box 500, Batavia, Illinois 60510

Invited Lectures given at the
Fourth Mexican School of Particles and Fields
Oaxtepec, Mexico
December 3-12, 1990

August 1991

HYPERONS: INSIGHTS INTO BARYON STRUCTURE*

Joseph Lach
Fermilab, P.O. Box 500
Batavia, IL 60510, USA

ABSTRACT

The baryon octet is composed mainly of hyperons. Modern high energy hyperon beams provide a tool for the study of hyperon static properties and interactions. Experiments with these beams have provided new insights into hyperon rare decays, magnetic moments, and interactions. These experiments provide us with insights into the strong, weak, and electromagnetic structure of the baryons.

1. The Hyperons

The modern point of departure for any discussion of the structure of elementary particles is the Standard Model. Figure 1 depicts the Standard Model and I note the three generations, each generation containing a doublet of quarks. Our familiar world is made of baryons composed of first generation quarks, the u and d doublet. Baryons containing an s quark are hyperons. This is an "after the fact" definition since hyperons were known long before the quark model. However, the quark model provides the context for our discussion.

The SU(3) combinations of the three lowest mass quarks to form baryons are depicted in Figure 2. Here I ignore, at least for the time being, the three higher mass quarks. I make the normal definition of hypercharge as the sum of baryon number and strangeness. Identifying electric charge as one half the hypercharge plus the third component of isotopic spin, I can now form the baryon octet and decouplet. The lowest mass spin 1/2 baryons are identified in Figure 2 as well as the lowest mass spin 3/2 baryons.

The lifetimes of the baryons are determined by the interactions and final states available to each of them. Strong interaction decays occur with lifetimes so short that even at high energies the hyperons do not move distances interesting to an experimenter. Within the octet all of the members are stable under the strong interactions; the rest - except for the proton - decay by way of the weak interactions. The Σ° can also decay electromagnetically, $\Sigma^\circ \rightarrow \Lambda^\circ \gamma$; the proton is stable. Among the lowest mass members of the decouplet only the Ω^- does not decay strongly. Table 1 summarizes the quark content and lifetimes of the long lived baryons; that is, those that do not have strong decays.

Much of the early data on hyperon static properties such as lifetimes, decay modes, etc. was extracted from low energy bubble chamber photographs. Figure 3 is a bubble

*This work was supported by the U.S. DOE under contract #DE-AC02-76CH03000.

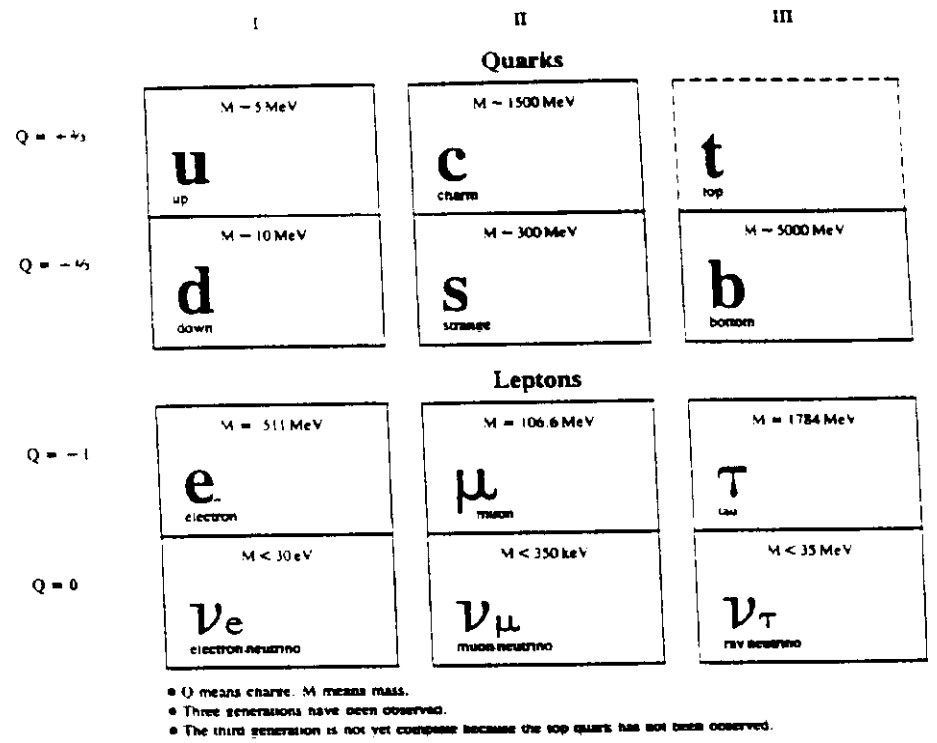

Figure 1. The Standard Model

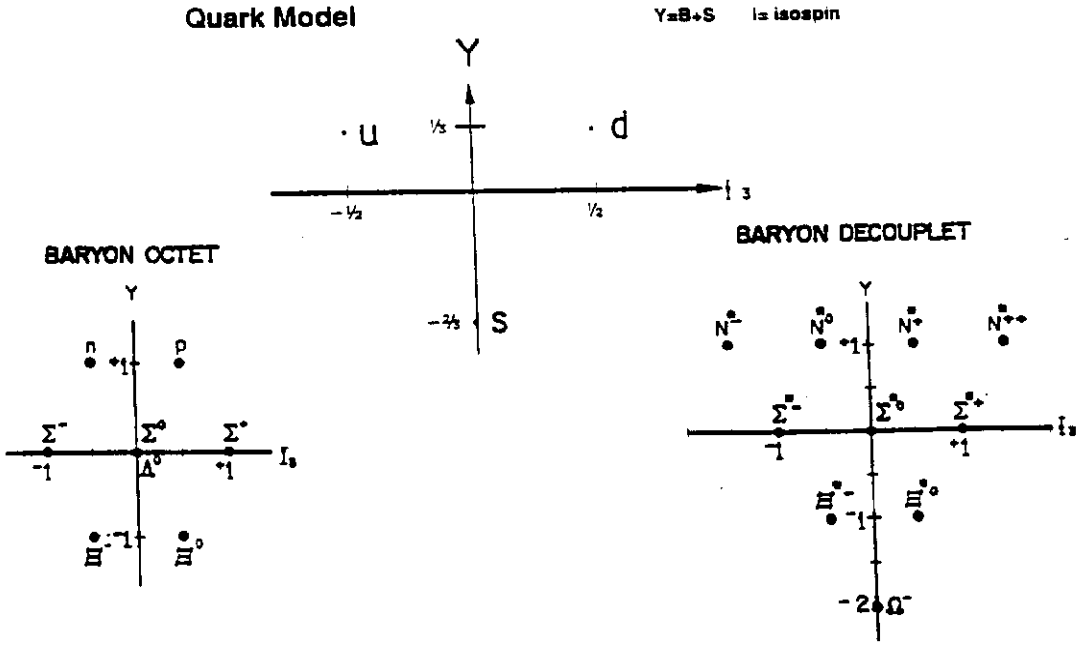

Figure 2. The Quark Structure of the Baryons

Table 1 The Long Lived Baryons.
Data from reference 1.

	Baryon	Quark Content	Mass MeV/c^2	Lifetime Sec
Octet				
	p	uud	938.27	stable
	n	udd	939.57	896
Hyperons	Λ°	uds	1115.63	2.632×10^{-10}
	Σ^+	uus	1189.37	7.99×10^{-11}
	Σ°	uds	1192.55	7.4×10^{-20}
	Σ^-	dds	1197.43	1.479×10^{-10}
	Ξ°	uss	1314.9	2.90×10^{-10}
	Ξ^-	dss	1321.32	1.639×10^{-10}
Decouplet				
	Ω^-	sss	1672.43	8.22×10^{-11}

chamber photograph taken from the thesis of Gershwin.[2] It shows a photograph from the Lawrence Berkeley Laboratory (LBL) 25 inch bubble chamber exposed to a 390 MeV/c K^- beam. The beam enters from the bottom of the picture and one sees an interaction identified as $K^-p \rightarrow \Sigma^+\pi^-$. One also sees the subsequent decay, $\Sigma^+ \rightarrow p\gamma$, and the photon converting to an electron-positron pair near the top of the photograph. The short dark track is the Σ^+ and the longer connected dark track is the proton. The production dynamics of the hyperon is well known from the study of low energy phase shifts.[3] The energy of the K^- beam was chosen to have the center of mass energy near the mass of the $Y_0^*(1530)$. This D-wave resonance interferes with the S-wave background to produce Σ^+ with about 37% polarization. This is a very important technique to study the spin structure of the hyperons.

The bubble chamber technique has serious drawbacks. One is limited to only a few tracks per picture, and the Σ^+ with its short path length does not curve appreciably in the magnetic fields available in bubble chambers. If the hyperons could be produced with decay lengths long enough to separate their production vertices from their decay positions then one would not be encumbered with the backgrounds of the production region. It is this fact which pushed the development of hyperon beams.

A hyperon beam makes use of the relativistic lifetime increase due to its high energy. If I have N_0 hyperons, I can write the number, N, which will not have decayed after traveling a distance l as

$$N = N_0 \exp(-l/l_d) \quad \text{where} \quad l_d = P\,\tau_0/m$$

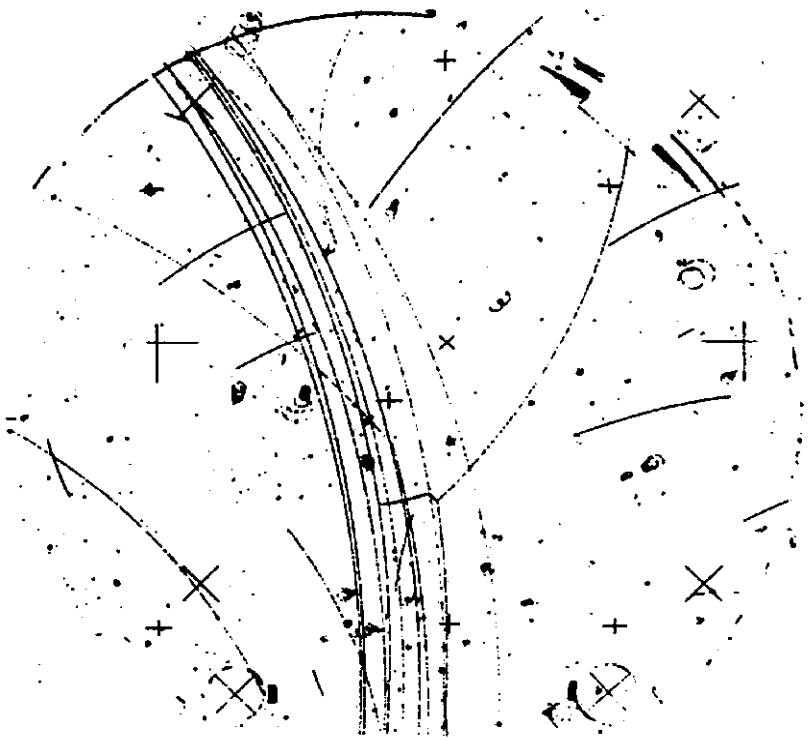

Figure 3. Interaction in LBL 25 inch bubble chamber showing $K^- p \rightarrow \Sigma^+ \pi^-$ and the subsequent decay $\Sigma^+ \rightarrow p\gamma$

Here P is the hyperon momentum, τ_0 is its proper lifetime (at rest relative to the observer), and m is its rest mass. In Figure 4, I plot the decay length as a function of momentum for hyperons of interest. The early hyperon beams using the Alternate Gradient Synchrotron (AGS) of Brookhaven National Laboratory (BNL) and the Proton Synchrotron (PS) of CERN had momenta of $\approx 10-20$ GeV/c. From figure 4, I note that this would give us decay lengths of only a couple of meters at best. Although, these were successes compared to previous techniques, it was not until the CERN Super Proton Synchrotron (SPS) and Fermilab that one saw their full impact.

Hyperon beams rely on the kinematics of hyperon production. The backgrounds to these beams are the general features of high energy proton collisions. Figure 5 shows photographs of 300 GeV protons interacting in the Fermilab 30 inch hydrogen bubble

chamber. Since only charged particle tracks are visible in a bubble chamber and since their curvature in the magnetic field is proportional to their charge and momentum, these pictures give us a good visualization of the reactions. Note in the top photograph that there seems to be a core of forward particles which may loosely be thought of as due to the fragmentation of the projectile. The fragmentation of the target gives rise to lower energy tracks, and one notes a large-angle heavily-ionizing track: a proton. The mean charge multiplicity[4] (the mean number of charged particles produced in an interaction) for inelastic events at this energy is 8.5 particles.

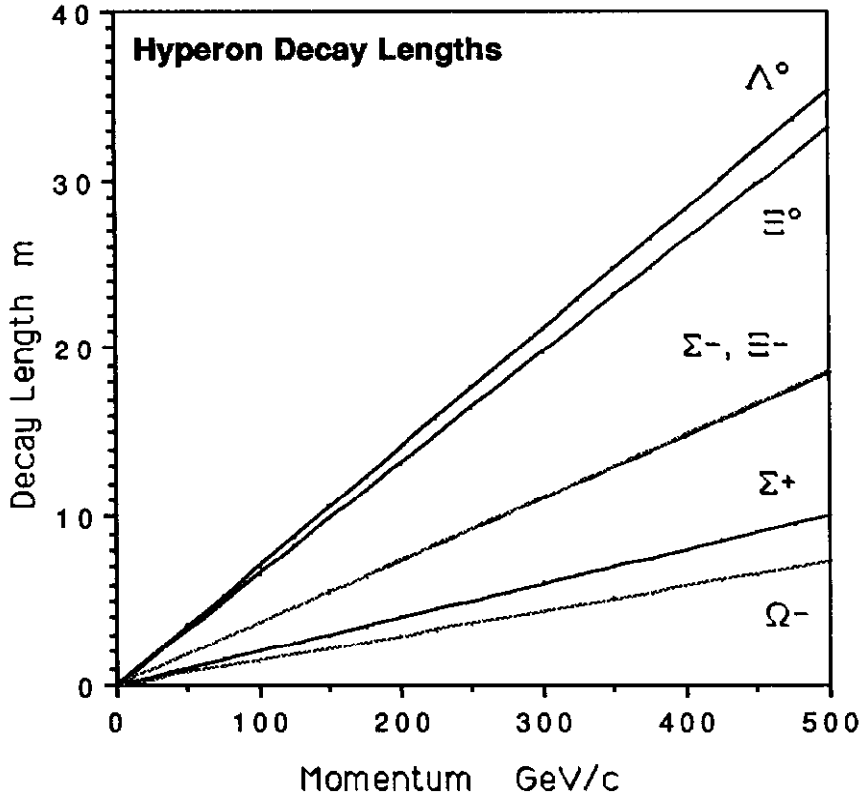

Figure 4. Hyperon Decay Length vs. Momentum

The lower photograph taken from the same run shows the production of two "vee" tracks. The "vee" indicates where the neutral particle decayed into charged secondaries. These are undoubtedly the decays of strange particles - most likely $K^{\circ} \rightarrow \pi^{+}\pi^{-}$ or $\Lambda^{\circ} \rightarrow p\pi^{-}$. Charged hyperon decays are more difficult to see in these photographs because they would appear as small "kinks" in a charged track. The task for the hyperon beam designer is to find a way of deflecting or interacting away most of the unwanted particles (pions, kaons, neutrons, etc.) and yet enhancing the kinematic region of maximum hyperon production.

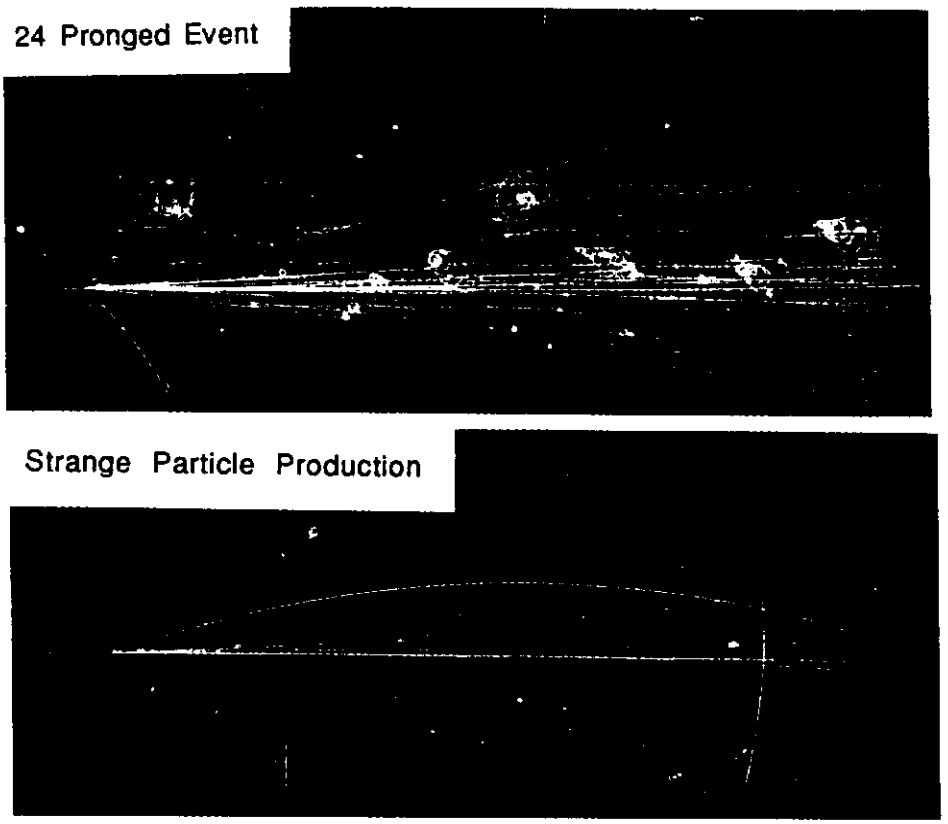

Figure 5. 300 GeV proton interactions in the Fermilab 30" bubble chamber

2. Hyperon Beams

There are a number of excellent reviews describing hyperon beams and the physics programs that have utilized them.[5-8]

What are the essential elements of a hyperon beam?

*Start with a high energy proton beam
*Interact the beam in a small target to produce hyperons
*Select particles produced in the forward direction - large x_F.
*Collimate in the other directions. Interact as many of the other secondary particles as practical, especially the pions before they can decay to muons.
*Magnetically select the desired momentum
*Do all of the above in as short a distance as possible to maximize the number of hyperons that survive. This puts a premium on

**high magnetic fields
**high resolution detectors
**high energy

In Figure 6, we see the essential elements of a hyperon beam. The Fermilab hyperon beam in Proton Center has a 7m long magnet, the hyperon magnet,[9] with a vertical magnetic field of about 3.5 T. The inner portion of the magnet containing the channel is removable and can be fitted with a curved channel appropriate for a charged beam or a straight channel for a neutral beam. A set of magnets upstream of the hyperon magnet allows for the angle of the proton beam impinging on the target to be varied either in the horizontal or vertical direction. This allows for the targeting angle to be varied between about ±4 mrad in either plane for 800 GeV incident protons. The transverse momentum, p_t, of the produced beam particle is just the product of the sine of the targeting angle and the hyperon momentum. Along with the Feynman x (x_F), it is used to characterize a hyperon beam.

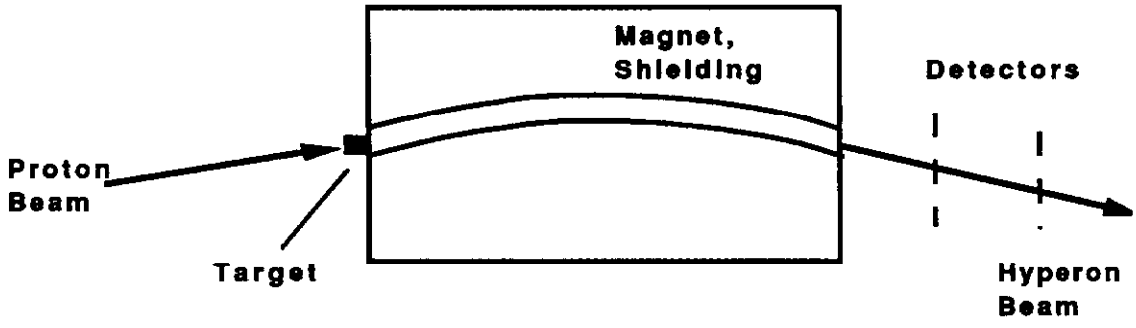

Figure 6. Essential Elements of a Charged Hyperon Beam

Following the hyperon magnet is a set of high resolution spatial detectors. In the earlier beams these were spark chambers and then proportional chambers; now silicon strip detectors are used. In a recent configuration, a Cu target of 0.5 mm full width in the horizontal plane coupled with 50 μm pitch silicon strip detectors resulted in momentum resolution of ≈0.2% ($\Delta p/p$) and angular resolution of ≈10 μrad.

An important consideration in the early charged hyperon beams was the identification of the hyperons before they decayed. Ĉherenkov detectors were used for particle identification in the early BNL AGS and CERN PS beams. Figure 7 shows the beam[10] configuration of the CERN PS beam.

A charged particle traveling with a velocity greater than the speed of light in a medium will emit Ĉherenkov radiation. The angle of the particle's Ĉherenkov radiation is given by

$$\cos \theta_c = 1/n\beta \quad \text{with } \beta = v/c$$

and n being the refraction index of the Ĉherenkov medium. In Figure 7 this counter is referred to as a DISC; that is, a differential isochronous Ĉherenkov detector. It is straightforward to calculate the angular separation of two Ĉherenkov rings produced by particles of mass m_1 and m_2, and momentum p

$$\Delta\theta_c = (m_1^2 - m_2^2)/(2p^2 \tan \theta_c)$$

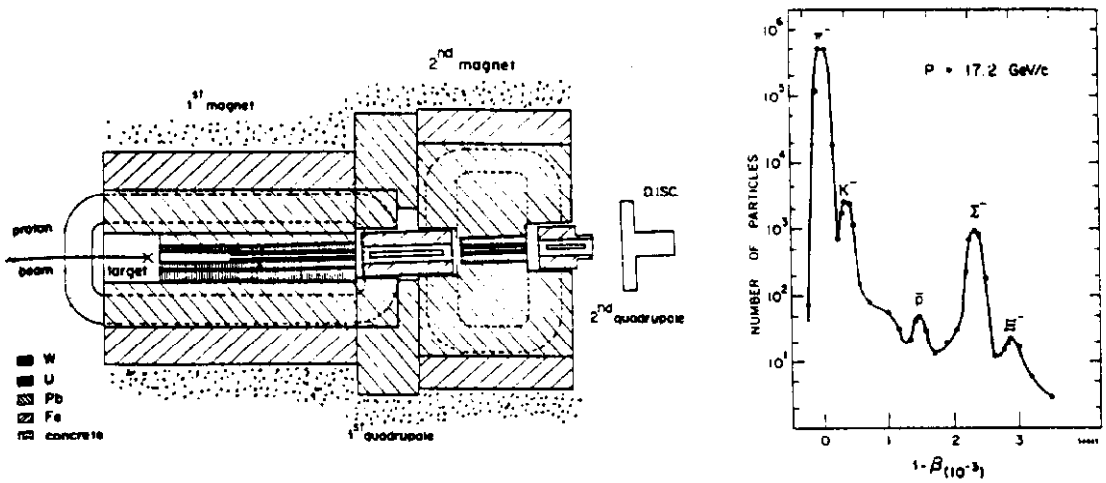

Figure 7 (a) Early CERN PS charged hyperon beam showing quadrupole focussing magnets and Ĉherenkov counter.
(b) Ĉherenkov counter pressure curve

Thus, the separation is larger at small θ_C. However, if one uses a phototube as a detector, the number of detected photoelectrons is given by

$$N = AL \sin^2\theta_C$$

where L is the path length in the medium. Thus, a compromise must be reached between these two conditions.

For the Ĉherenkov detector to work the angular spread of the beam must be smaller than the separation of the Ĉherenkov angles of the particles to be identified. Figure 7 shows the use of magnetic quadrupole lenses to render the beam more nearly parallel to help this separation. In the Figure 7 beam the Ĉherenkov medium was a gas whose pressure, and hence refractive index, could be easily changed. In the same figure is a pressure curve which shows the copiously produced π^- and K^- particles. Clearly visible are the $\bar{p}$, Σ^-, and Ξ^-, which can now be incorporated into an electronic trigger. This was an important advancement in producing a useful hyperon beam.

The above beam was soon followed by a higher energy beam[11,12] at BNL, constructed by a group from Fermilab and Yale. Its configuration is shown in Figure 8. The 29 GeV proton beam impinged on a small metal target and the resulting 23 GeV/c beam was transported through a small tungsten lined channel. A DISC type Ĉherenkov counter was not used in this beam; however, the interior of the channel was coated with a reflective material and filled with a gas to make a threshold Ĉherenkov counter which was sensitive to charged pions, but not particles of baryonic mass.

The hyperon momentum and direction were determined by the magnetic channel and the high resolution chambers just downstream of it. The downstream analyzing magnets and spark chambers determined the trajectory of one of the charged decay particles. For two body decays the reaction could be readily identified even though the trajectory of the neutral

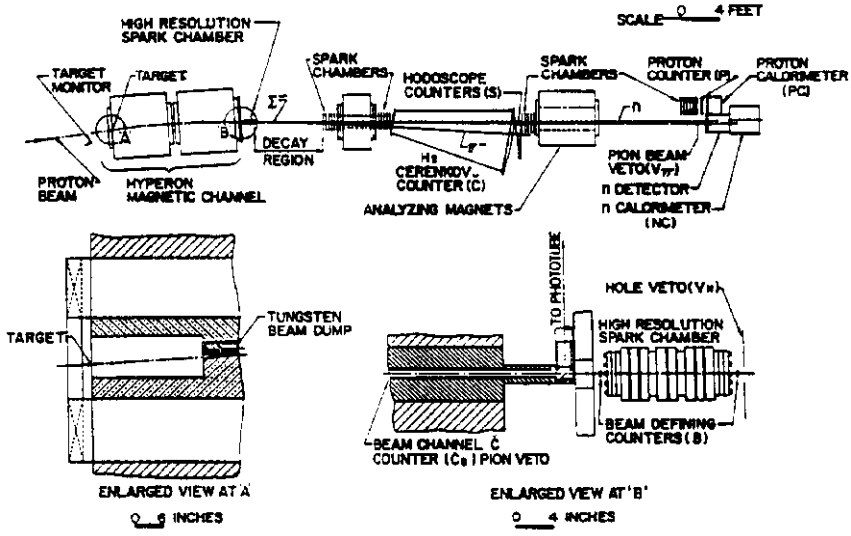

Figure 8. High Energy Negative Hyperon Beam at BNL.

particle was not measured. Figure 9 shows the reconstructed hyperon masses[12] measured with this beam.

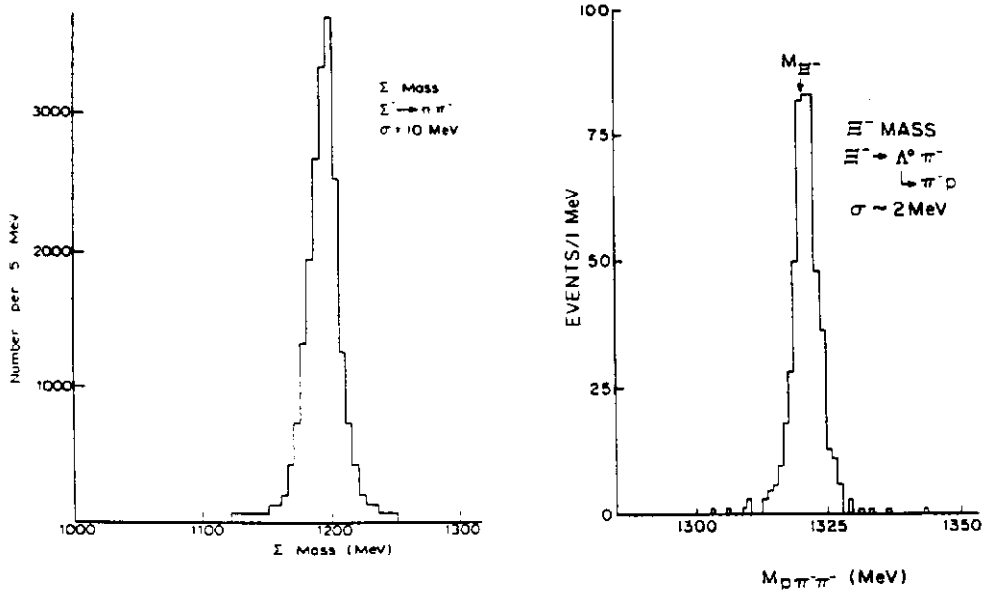

Figure 9. Σ^- and Ξ^- reconstructed mass from the Yale - Fermilab beam at BNL

These early hyperon beams provided the first systematic measurements of hyperon fluxes and provided the "engineering" measurements for later beams. Figure 10 is an early measurement[12] of these hyperon fluxes and a comparison with production of charged pions and kaons. This comparison is important since these are the contaminants to the hyperon beam and their numbers will usually limit rates in the apparatus designed to study hyperon properties.

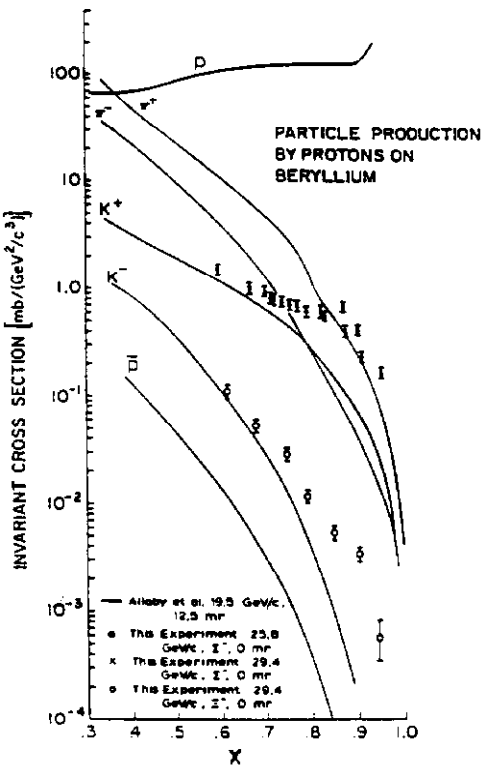

Figure 10. Hyperon Production Comparison Cross section vs. x_F

Figure 10 deserves some comments. Plotted is the measured production cross section as a function of Feynman x, x_F. For this case, to a good approximation, it is just the ratio of the secondary particle momentum divided by the incident proton momentum. These yields have all been corrected for decay losses and extrapolated back to the production target. One notes a surprising fact: at large x_F the yield of Σ^- is greater than that of π^-, and that of Ξ^- is greater than that of K^-! This demonstrated that hyperons are produced copiously at high energies and are $\approx 10\%$ of all produced particles. It also showed the desirability of yet higher energy beams so that these high yields could be realized well downstream of the target as was indicated by Figure 4.

Table 2 gives a short description of the major charged hyperon beams. The successful operation of beams at CERN and BNL was followed by beams at the major new high energy machines at CERN and Fermilab. In Table 2, I try to give some of the salient features of these beams. This is not intended to be a complete list, but to give an overview of the properties of the major beams.

Table 2

Charged Hyperon Beam Characteristics

	CERN PS 1969	BNL AGS 1970	CERN SPS 1978	Fermilab PC 1981
Incident Protons	24 GeV	29 GeV	200-400 GeV	400 GeV
Flux per pulse	$\approx 10^{11}$	$\approx 1.5\text{-}10^{11}$	$\approx 4\text{-}10^{10}$	$\approx 10^{9}\text{-}10^{12}$
Secondary Momenta GeV/c	13-20	17-26	70-140	100-350
Length meters	3	4.4	12	10
Fluxes per pulse	50 Σ^- 1 Ξ^-	200 Σ^- 2 Ξ^-	4000 Σ^- 400 Ξ^- 2 $\overline{\Sigma}^-$ 0.1 Ω^- 50 Σ^+ 2 $\overline{\Xi}^+$	100,000 Σ^- 2000 Ξ^- 20 $\overline{\Sigma}^-$ 0.5 Ω^- 1000 Σ^+ 20 $\overline{\Xi}^+$ 0.1 $\overline{\Omega}^+$
Physics Results	Σ^-, Ξ^- Fluxes Σ^-p, σ_t, $\overline{d\sigma/dt}$ $\Sigma^- \to n\, e^-\, \overline{\upsilon}$	Σ^-, Ξ^- Fluxes Σ^-p, $\overline{d\sigma/dt}$ $\Sigma^- \to n\, e^-\, \overline{\upsilon}$ $\Sigma^- \to \Lambda\, e^-\, \overline{\upsilon}$ $\Sigma^- \to Y^*$	Fluxes Ω^-, BR, Flux Leptonic Decays Y^* Physics Charm	Fluxes Leptonic Decays Magnetic Moments
Use Polarization?	No	No	No	Yes

How can we visualize the dynamics of hyperon production? From Figure 10, we can see that the production of Σ^- and Ξ^- is copious in the forward direction. Diagrams which emphasize leading particle effects - mechanisms in which one or more of the projectile's constituent or valence quarks are incorporated into the produced hyperon - probably play a significant role. Each of the two diagrams illustrated in Figure 11 has the produced hyperon containing some of the constituent quarks of the projectile. It follows from momentum conservation that in the sequential decay of the first diagram, the heavier particle would absorb most of the laboratory momentum. These diagrams, which have the hyperons as "leading particles," would each contribute to the observed large x_F distribution of the hyperon.

Hyperon beams utilize hyperons produced inclusively. The initiating proton beam strikes a target and only particles produced in a very limited angular and momentum range are observed. This means that we know very little about the detailed mechanism of the production. We do not know in a particular interaction what other particles are produced, what are their multiplicity distributions, correlations, etc.

Many of the same design questions I have discussed for charged hyperon beams also apply to neutral beams. The curved channel of Figure 6 becomes a straight channel but one

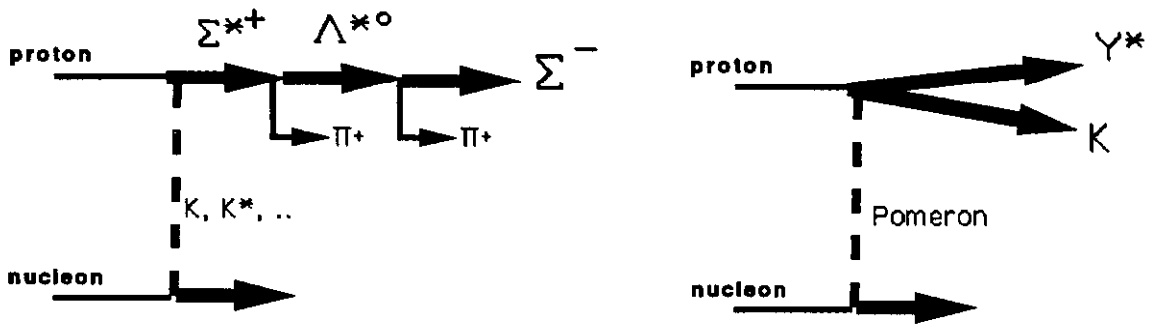

Figure 11. Diagrams which may contribute to leading hyperon production

still needs a high magnetic field to sweep away unwanted charged particles, high resolution detectors, good shielding, etc. The large magnet built for the Fermilab Proton Center charged hyperon beam[8] has a removable central channel. The original channel was lined with tungsten, and had a radius of curvature appropriate for transmitting a 350 GeV/c particle at its maximum magnetic field of about 3.5 T. Although the full magnet weighs about 400 tons, this central channel can be readily removed and replaced by either a straight channel suitable for a neutral beam or a curved channel with a larger radius of curvature suitable for a higher momentum charged beam.

Of course, in a neutral beam, there is no momentum selection; one accepts all energies and particle types. One has not only Λ° particles but also neutrons and photons of all momenta produced in the target. Reference 6 is an excellent review of the Fermilab neutral hyperon beam program. Figure 12, taken from this work, is a schematic layout of such a beam. The signature of a detected Λ° is the decay $\Lambda^\circ \rightarrow \pi^- p$, which has the characteristic "vee" signature. In Figure 12, note the ability to change the incident proton beam direction and hence vary the hyperon production angle. Note also the large targeting magnet, the evacuated decay region, and the spectrometer and Ĉherenkov detector to measure the momenta and identify the hyperon decay products.

An important constraint on identifying a Λ° produced in the target is that the reconstructed Λ° momentum points to the target. However, in the decay $\Xi^\circ \rightarrow \Lambda^\circ \pi^\circ$, the Λ° does not originate in the target and would not in general point back to it. Supplemented with lead glass arrays for photon identification from the decay $\pi^\circ \rightarrow \gamma\gamma$, this has proved an effective method for Ξ° identification. Although there is a large body of information on hyperon production, it is far from complete. The most detailed studies have been done for the Λ° system, and this is described in considerable detail in reference 6.

Figure 13 shows the production cross sections of Λ° and $\overline{\Lambda}^\circ$ produced at various production angles with a 400 GeV proton beam on a beryllium target. Note that at a given angle and x_F, the production of the $\overline{\Lambda}^\circ$ is orders of magnitude larger. Careful, the units for the Λ° are mb while those of the $\overline{\Lambda}^\circ$ are μb! One also notes that the Λ° production is large at large values of x_F as would be expected for leading particle production. Similar graphs are presented for Ξ° and $\overline{\Xi}^\circ$ production in reference 6.

The general shapes of these distributions do not change very rapidly as a function of incident beam momentum. There is only a slight dependence on the target material, but

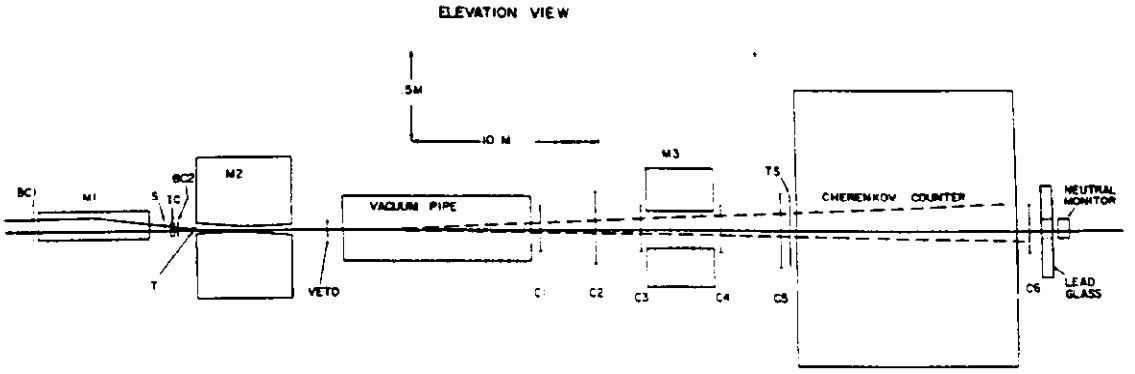

Figure 12. Early spectrometer for a neutral hyperon beam. Note the target (T) location and chambers (BC and BC2) to monitor incident beam positions. C1-C6 are wire chambers used to reconstruct hyperon decay products.

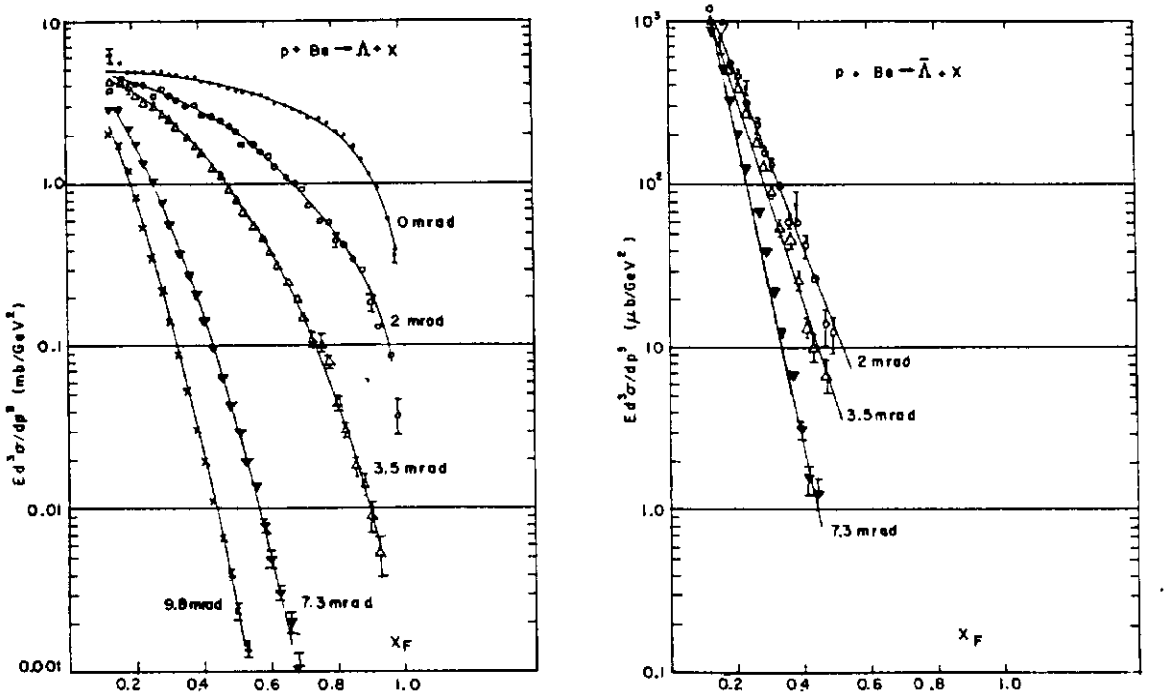

Figure 13. Cross sections for the production of Λ° and $\overline{\Lambda}^\circ$ as a function of x_F for various production angles at 400 GeV.

there is a large dependence on production angle, or P_t. One concludes from this behavior that the hyperons exhibit a leading particle behavior but the antihyperons, having no quarks in common with the projectile, do not.

3. Measurement of $d\sigma/dt$, σ_t, Y^* Production

Tests of the quark model as it related to the high energy strong interactions of the baryons were of particular interest at the time of the early hyperon beams. Of particular

importance was the "size" of the baryon as a function of its quark content. Measurements of baryon total and elastic differential cross sections, σ_t and $d\sigma/dt$, at high energies received much attention. Here t is the four momentum transfer between the initial projectile and the final state hyperon.

Figure 14 shows a typical apparatus for the measurement[13] of σ_t and $d\sigma/dt$. This is a classical transmission experiment. One sequentially inserts a set of targets into the hyperon beam and records the interaction rate. Shown are a hydrogen, a deuterium, and an evacuated cylinder of similar dimensions, a "blank." One measures the momentum and direction of each incident particle, then whether it was absorbed or scattered, and if scattered the scattering angle.

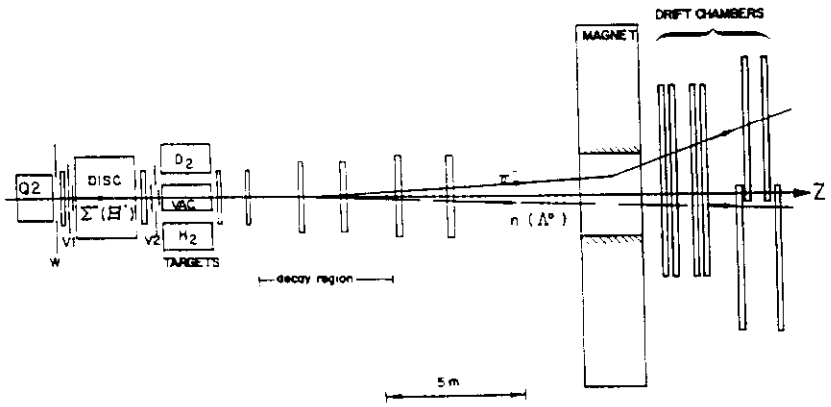

Figure 14. Apparatus for the measurement[13] of σ_t and $d\sigma/dt$ at the CERN SPS. The hyperon production target is off the diagram to the left.

The measurements of $d\sigma/dt$ and σ_t are important in understanding the size and shape of the hyperons at high energies. The earliest hyperon beam measurements of $d\sigma/dt$ were done at the CERN PS and at BNL AGS, and data for $\Sigma^- p$ scattering is shown[5,14] in Figure 15. The fact that the logarithmic extrapolated $d\sigma/dt$ does not go through the optical point indicates either that the logarithmic slope is not linear - as is the case for pp elastic scattering - or that there is a problem with the normalization.

The total cross sections measurements[13] in Figure 16, which were done at the CERN SPS, are the highest momentum (≈ 140 GeV/c) hyperon total cross section data available. Note the slow rise of the cross section with momentum. The hydrogen and deuterium data can be analyzed to yield the proton and neutron data separately, and from them fits can be made to various quark model predictions. It is important that these measurements be carried out at high energies where one is far removed from s-channel resonances.

From very early data on the measurements of the total cross sections, it was clear that particles containing a strange quark had smaller total cross sections than their non-strange counterparts. In the simplest picture one can write

$$\sigma t(\pi^- p) - \sigma_t(K^- p) = \Delta$$

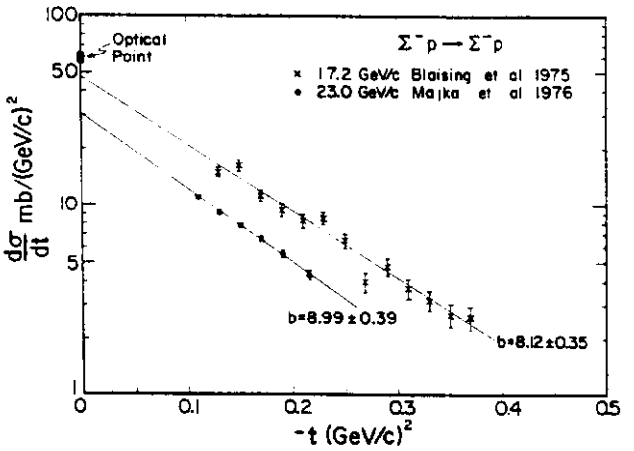

Figure 15. Early measurements of $d\sigma/dt$.

where one finds that $\Delta \approx 4$ mb. One can compare the effects of adding one or more strange quarks

$$\sigma t(pp) - \sigma_t(\Sigma^- p \text{ or } \Lambda^\circ p) = \Delta$$

$$\sigma t(pp) - \sigma_t(\Xi^- p) = 2\Delta$$

$$\sigma t(pp) - \sigma_t(\Omega^- p) = 3\Delta$$

Although no measurements exist for $\sigma_t(\Omega^- p)$, the model gives reasonable agreement with data. The reader is referred to reference 13 for details. Embellishments of this model have problems with agreement at about the 1% level. It would be straightforward to extend these measurements of total cross sections to the momentum range of $\approx$200-600 GeV/c for not only Σ^-, Σ^+, and Ξ^-, but also for $\overline{\Sigma^-}$ using the Fermilab hyperon beam.

High energy hyperon beams are ideal tools for the study of excited hyperon states. These are states which are produced in strong interactions, decay through them, and are observed as resonances. They possess a rich structure since the baryon octet and decouplet shown in Figure 2 are only the ground states. The understanding of the properties of these excited states is important for understanding the nature of the quark forces. Excited hyperon states were observed[15] from the first charged beams at CERN and BNL. However, it was with the CERN SPS beam that more detailed studies of these states were conducted. These included studies of S=-2 states.[16]

The most interesting was the discovery of the first S=-3 excited states[17] of the Ω^-. With the CERN SPS hyperon beam,[8] one could identify the incident hyperon as a Ξ^-, and one could investigate the products resulting from its interaction in a target. Modifications to the detector were the addition of more planes of wire chambers to be able to measure and sort out the many additional tracks present in the event, Cherenkov detectors to identify the interaction products, and lead glass (or some other photon identifier). With that one is able

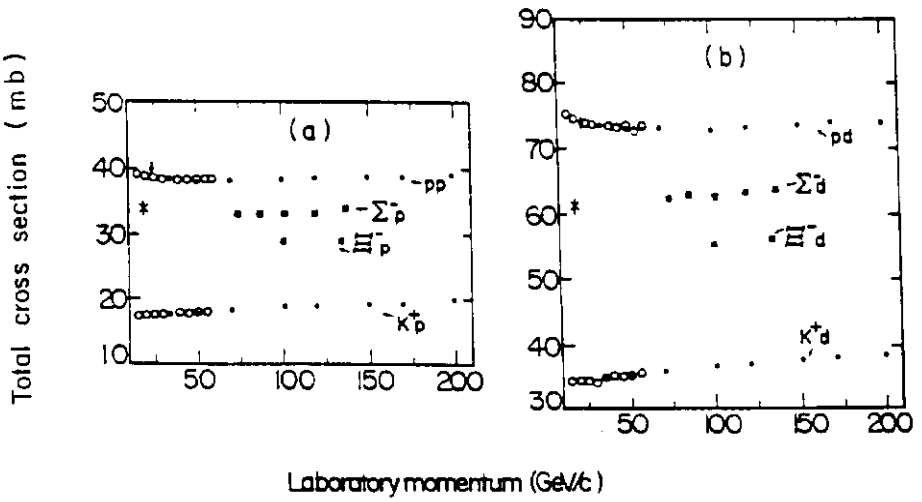

Figure 16. Hyperon total cross section as a function of momentum

to reconstruct complicated decay chains such as

$$\Omega^{*}\rightarrow\Xi^{-}\ \pi^{+}\pi^{-}$$
$$\Xi^{-}\rightarrow\Lambda^{\circ}\pi^{-}$$
$$\Lambda^{\circ}\rightarrow\pi^{-}p$$

4. Hyperon Polarization

The hyperons of the octet shown in Figure 2 all have spin 1/2 and, except for the Σ°, have their major decays modes mediated by the weak interactions. This means that information from the distribution of their decay products can be used to determine their spin direction. I illustrate this in Figure 17 where I schematically represent the polarized decay of a $\Lambda^{\circ}\rightarrow p\pi^{-}$. The Λ° here is totally polarized having its spin direction in the +z direction. The spin parity (J^{P}) assignment[1] of the Λ° is $J^{P}=1/2^{+}$. If parity was conserved in its decay - **it is not** since it decays through the weak interactions - we could write the parity of the decay products

$$P(\Lambda^{\circ}) = P(\pi^{-})\ P(p)\ (-1)^{l}$$

In this notation l is the angular momentum of the final state, the parity of the π^{-} is $P(\pi^{-})=-1$, and $P(p)=+1$.

Parity and angular momentum conservation would only allow the p-state, l=1. Angular momentum conservation alone allows either the s or p-state, l= 0 or 1. Thus, we can equate the angular momentum part of the initial spin 1/2 wave function to the sum of the two possible final wave functions

$$\Psi_{1/2}= \alpha_{p}\{\sqrt{2/3}\ Y_{11}\chi_{-1/2} - \sqrt{1/3}\ Y_{10}\chi_{+1/2}\} + \alpha_{s}\ \{\ Y_{00}\chi_{+1/2}\}$$

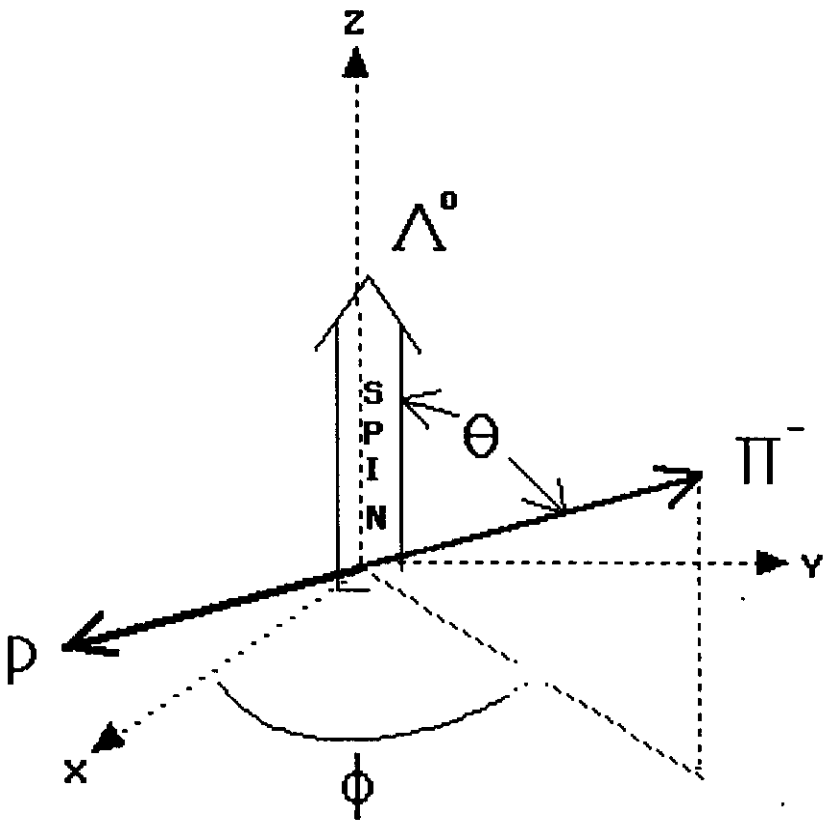

Figure 17. Decay of a polarized Λ°

We can form the intensity

$$I=|\Psi|^2 = 1/4\pi \{|\alpha_S|^2 + |\alpha_P|^2 - 2\,\mathrm{Re}\,\alpha_S\alpha_P^* \cos\theta\}$$

which we can rewrite as

$$I \approx 1 + \alpha \cos\theta \quad \text{where} \quad \alpha = -2\mathrm{Re}\ \alpha_S\alpha_P^*/(|\alpha_S|^2 + |\alpha_P|^2)$$

It is easy to see that if the initial hyperon was not totally polarized we would write

$$I \approx 1 + \alpha P \cos\theta$$

where **P** is the hyperon polarization. Note that we need both s and p waves in the final state to get an $\alpha \neq 0$.

Referring to Figure 17 we define an asymmetry

$$A = 2(N\uparrow - N_\downarrow)/(N_\uparrow + N_\downarrow)$$

where $N_\uparrow$ is the number of decays having the proton in the +z direction and $N_\downarrow$ is the number of decays having the -z direction. We can write this in terms of αP by noting that

$$N_\uparrow \approx \int_0^{\pi/2} (1+\alpha P \cos\theta)\, d(\cos\theta) = 1 + \alpha P/2$$

$$N_\downarrow \approx \int_{\pi/2}^{\pi} (1+\alpha P \cos\theta)\, d(\cos\theta) = 1 - \alpha P/2$$

Hence $A=\alpha P$. Now we know how to go from physical measurements of the number up and the number down to the product of αP.

The physics of the decay is contained in α. If we just wish to measure a polarization or see the spin direction precess by a magnetic field we need not be concerned how nature gave us α; we can just use it. Note that we measure asymmetries, hence the product of α and **P**. We need to have them both nonzero to measure a spin direction. The larger the value of α, the easier it is to measure A and hence the polarization.

Table 3 is a list[1] of some of the more important hyperon decay modes, branching ratios, and α parameters for these decays.

Table 3. Hyperon Decay Properties

Decay Mode	**BR %**	α
$\Sigma^+ \to p\pi^\circ$	51.6	-0.980±0.019
$\Sigma^+ \to n\pi^+$	48.3	0.068±0.013
$\Sigma^- \to n\pi^-$	99.8	-0.068±0.008
$\Sigma^- \to ne^-\bar{\upsilon}$	0.1	-0.519±0.104
$\Lambda^\circ \to p\pi^-$	64.1	0.642±0.013
$\Lambda^\circ \to n\pi^+$	35.7	0.65±0.05
$\Xi^\circ \to \Lambda^\circ\pi^\circ$	100.	-0.411±0.022
$\Xi^- \to \Lambda^\circ\pi^-$	100.	-0.456±0.014
$\Omega^- \to \Lambda^\circ K^-$	67.8	-0.026±0.026
$\Omega^- \to \Xi^\circ\pi^-$	23.7	0.09±0.14
$\Omega^- \to \Xi^-\pi^\circ$	8.6	0.05±0.21

From Table 3 we see that α for the various decay modes can assume a wide range of values. The decay $\Sigma^+ \to p\pi^\circ$ has α near its maximum negative value, making it easy to measure the Σ^+ polarization through this decay mode. The decay $\Sigma^- \to n\pi^-$ has a small but

clearly non-zero value of α making it necessary to have a large data sample and good control of systematic errors to get a measurement of its polarization.

In decays such as $\Xi^- \to \Lambda^\circ \pi^-$, where one also observes the subsequent decay $\Lambda^\circ \to p\pi^-$, information about the spin direction of the Ξ^- is contained in the decay distribution[6,18-20] of the decaying Λ°. Using the standard formalism[18,19] we can write

$$\beta = 2\ \mathrm{Im}\ \alpha_S \alpha_P^* / (|\alpha_S|^2 + |\alpha_P|^2)$$

$$\gamma = (|\alpha_S|^2 - |\alpha_P|^2) / (|\alpha_S|^2 + |\alpha_P|^2) .$$

We now can express the magnitude of the Λ° polarization

$$P_\Lambda = [(\alpha_\Xi + \hat{\Lambda}\cdot P_\Xi)\hat{\Lambda} - \beta_\Xi(\hat{\Lambda}\times P_\Xi) - \gamma_\Xi \hat{\Lambda}\times(\hat{\Lambda}\times P_\Xi)]/(1+\alpha_\Xi \hat{\Lambda}\cdot P_\Xi)$$

where $\hat{\Lambda}$ is the Λ° direction in the Ξ^- center of mass. Under time reversal invariance, assuming there are no final state interactions, and using the relation

$$\alpha^2 + \beta^2 + \gamma^2 = 1$$

it can be shown that $\beta = 0$. We can then write a somewhat simpler relation for P_Λ

$$P_\Lambda = [(\alpha_\Xi + (1-\gamma_\Xi)\hat{\Lambda}\cdot P_\Xi)\hat{\Lambda} + \gamma_\Xi P_\Xi)]/(1+\alpha_\Xi \hat{\Lambda}\cdot P_\Xi)$$

The extraction of the Ξ^- polarization is still tedious but straightforward, and must be done iteratively.

From Table 3, we see that for Ω^- decays the values of α are all small and consistent with zero. In this case we must use the information from the subsequent Λ° decay to determine the parent polarization. Note that one can still measure the α parameters for the Ω^- decay even if the Ω^- is not polarized.[8] This is further complicated by the fact that the Ω^- has spin =3/2. However, similar procedures as for the Ξ^- decay have been developed.[21]

Significant hyperon polarization was detected in the early Fermilab neutral hyperon beam.[22] Figure 18 shows this data for Λ° and $\overline{\Lambda}^\circ$ produced by 400 GeV protons. The polarization is plotted as a function of the transverse momentum, p_t, of the produced hyperon relative to the incident proton momentum. Note that since both the incident proton beam and the target are unpolarized, rotational symmetry require there be no polarization of the produced hyperons at $p_t = 0$.

The clear evidence (Figure 18) that Λ° is produced with significant polarization but that $\overline{\Lambda}^\circ$ is not polarized came as a surprise.

An argument had been made that strong interaction polarization effects should disappear at high energies. Roughly it went as follows. Polarization is an interference effect. To have a significant polarization requires two states that are large and which will interfere. At higher energies an increasingly larger number of angular momentum states

will participate and it will be unlikely that any two are dominant. The data of Figure 18 speak to the contrary.

As I have pointed out earlier, the Λ° is a leading particle and the $\overline{\Lambda}^\circ$ is not. Might this be significant? It must be kept in mind that these are inclusive measurements and we only measure one of the reaction products. We do not know if the Λ° was produced directly as a Λ° or was produced as a Σ° which then decayed $\Sigma^\circ \rightarrow \Lambda^\circ \gamma$. For that matter we do not know if the Λ° (or Σ°) was produced as a Y^* resonance which decayed strongly to the Λ° (or Σ°).

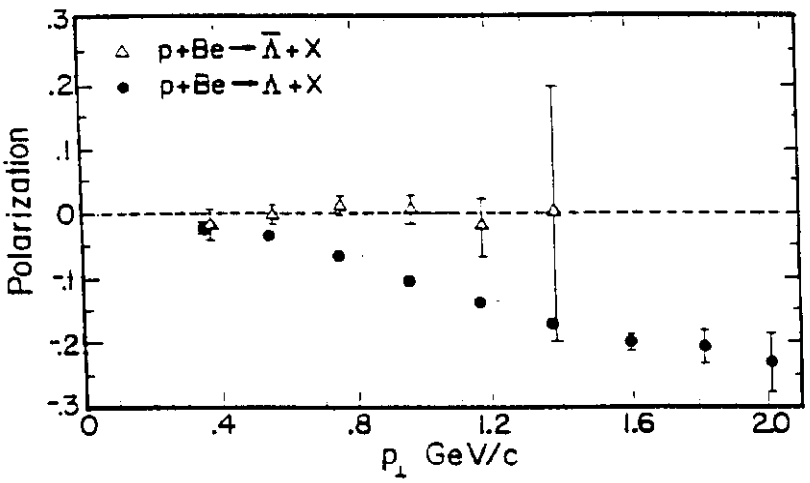

Figure 18. Λ° and $\overline{\Lambda}^\circ$ polarization as a function of p_t

Figure 19 shows the measured polarization of some other hyperons. Plotted here is the polarization as a function of the hyperon momentum at a fixed production angle. Since $p_t = P \sin\theta$, where P is the hyperon momentum and θ the production angle, the horizontal axis is proportional to p_t. These are all produced by 400 GeV protons. Significant polarization seems to be a general property of hyperon production at high energies.

One sees each of the hyperons being produced with polarization of $\approx 10\text{-}20\%$ at $p_t \approx 1$ GeV/c. The fact that early experiments had shown $\overline{\Lambda}^\circ$ to be unpolarized where in the same kinematic range Λ° was polarized lent credence to the idea that polarization is a leading particle effect. However, recent data have cast great doubt on this picture. Measurement of the $\overline{\Xi}^+$ polarization by the Fermilab E756 group[23] has shown it to be polarized by about the same amount as the Ξ^-. This data is shown in Figure 20. New preliminary data reported by the Fermilab E761 group at the 1991 American Physical Society meeting in Washington indicates that the $\overline{\Sigma}^-$ is also produced with $\approx 10\%$ polarization. Both sets of data used an 800 GeV proton beam. A Be target was used in E756, a Cu target in E761. The nature of the target material does not seem to have a major effect on hyperon production. Pondrom[6] has a good summary of target material dependence of hyperon production and polarization data.

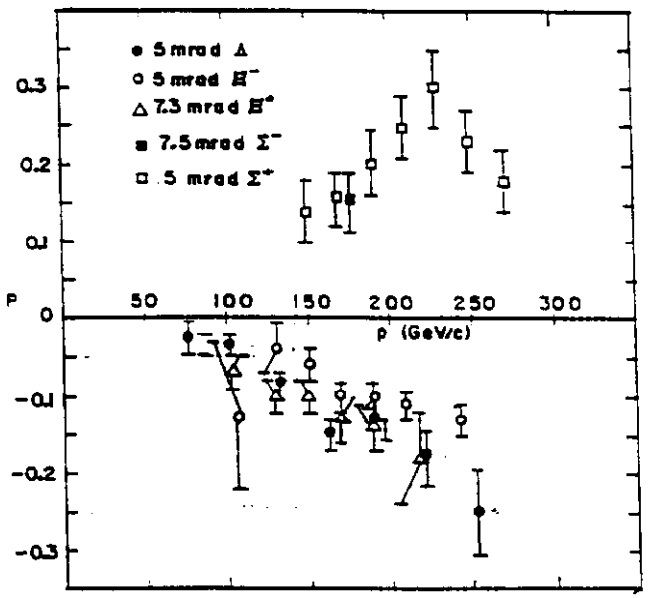

Figure 19. Polarization of other hyperons. Plotted is the polarization vs. hyperon momentum at fixed angles. The horizonatal axis is thus proportional to p_t. Figure from H.D. Diehl thesis.[35]

Can we see any pattern to hyperon polarization? Figure 21 displays the valence quark diagrams for the reactions we have discussed. I have separated them into three columns corresponding to whether the produced hyperon (or antihyperon) retains zero, one, or two of the projectile's valence quarks. In our notation for the antiparticles, we adopt the convention that the written sign is the electrical charge of the particle under consideration. Thus, for the antiparticle of the Ξ^- we write $\overline{\Xi}^+$, not $\overline{\Xi}^-$.

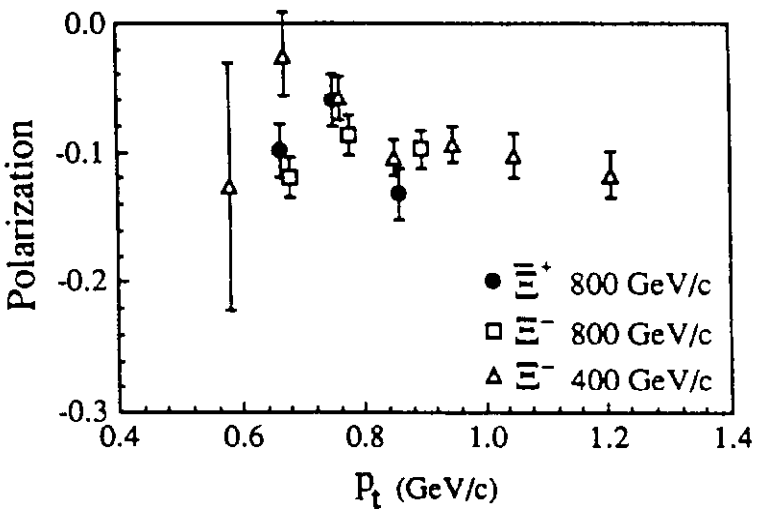

Figure 20. Ξ^- and $\overline{\Xi}^+$ polarization From Reference 23

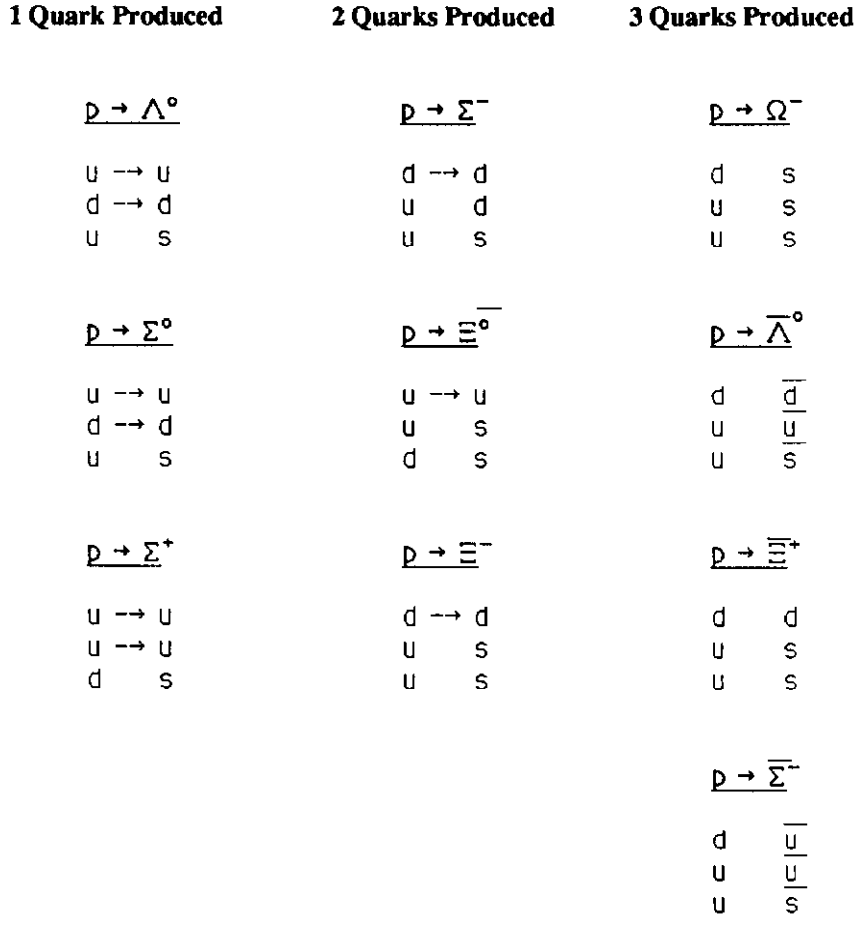

Figure 21. Quark Level Diagrams For Hyperon Production

Perhaps some clues may become evident if we look at the spin structure of the final state hyperons. Heller[24] pointed out that by examining the SU(6) wave functions and assuming that the produced s quark carries the polarization, one could infer that the polarization of the Σ^+ and the Σ° should be of opposite sign and 1/3 of the Λ° polarization. The sign is indeed opposite but the factor of 1/3 does not seem to hold (is the Λ° produced as Λ° or Σ° or Y^* states?).

To see this we take the SU(6) quark spin wave functions from any modern text or the early paper[25] of Franklin. These are shown in Figure 22. In the Λ° wave function, since the u and d quarks are in a singlet state, the spin of the Λ° is the spin direction of the s quark. The spin states of the Σ's are all triplets.

We can now take these wave functions and try to rewrite the valence quark diagrams that are shown in Figure 23. In addition to the production of hyperons by protons, other high energy data is included on polarized hyperon production by kaons and antiprotons.[26]

In Figure 23, using the wave function of Figure 22, I have noted the spin configurations of the hyperons. I have also noted the polarization directions of the produced

Triplet state

$$B\uparrow : \sqrt{2/3}\, a_1\uparrow\, a_2\uparrow\, b\downarrow - \sqrt{1/6}\, (a_1\uparrow\, a_2\downarrow + a_1\downarrow\, a_2\uparrow)\, b\uparrow$$

B	a_1	a_2	b
p	u	u	d
n	d	d	u
Σ^+	n	u	s
Σ^-	d	d	s
Σ°	u	d	s
Ξ°	s	s	u
Ξ^-	s	s	d

Singlet State

$$\Lambda^\circ\uparrow:\ 1/\sqrt{2}\ (u\uparrow\, d\downarrow - u\downarrow\, d\uparrow)\, s\uparrow$$

$$\Omega^-\uparrow:\ s\uparrow\, s\uparrow\, s\uparrow$$

Figure 22. Baryon SU(6) Quark Spin Wave Functions

hyperons. If one ignores the antihyperons, one notes that the s quark is always produced with its spin down.

Let me also mention two other approaches to the polarization question. One is that of Gustafson[27] (Lund model) whose model assumes $q\bar{q}$ pairs are produced from the sea via the breaking of a QCD string but conserving local angular momentum. DeGrand and Miettinen[28] propose two simple rules: quarks which gain longitudinal momentum combine with spins down; quarks which lose longitudinal momentum combine with spins up. This is equivalent to a Thomas precession and a spin orbit coupling. Both models explain much of the data. The magnitudes of some of the polarizations are at odds with each of the models. None of them can explain the polarizations of the antihyperons. A recent review by P. Kroll[29] is recommended although it was done before the polarizations of the $\bar{\Xi}^+$ and $\bar{\Sigma}^-$ were measured.

The role of the Ω^- has been a special one in the quark model picture. Its prediction by Gell-Mann and Okubo[30] and subsequent discovery at BNL[31] was a key test of the quark model. Just three strange quarks aligned to form a spin 3/2 object, it is the simplest hyperon that is accessible to the experimentalist. It is also the only member of the decouplet that does not decay strongly, making it the only s=3/2 object of a charged hyperon beam. Its short lifetime (compared to the other charged hyperons) and low production cross section have pushed beams to higher energies and intensities.

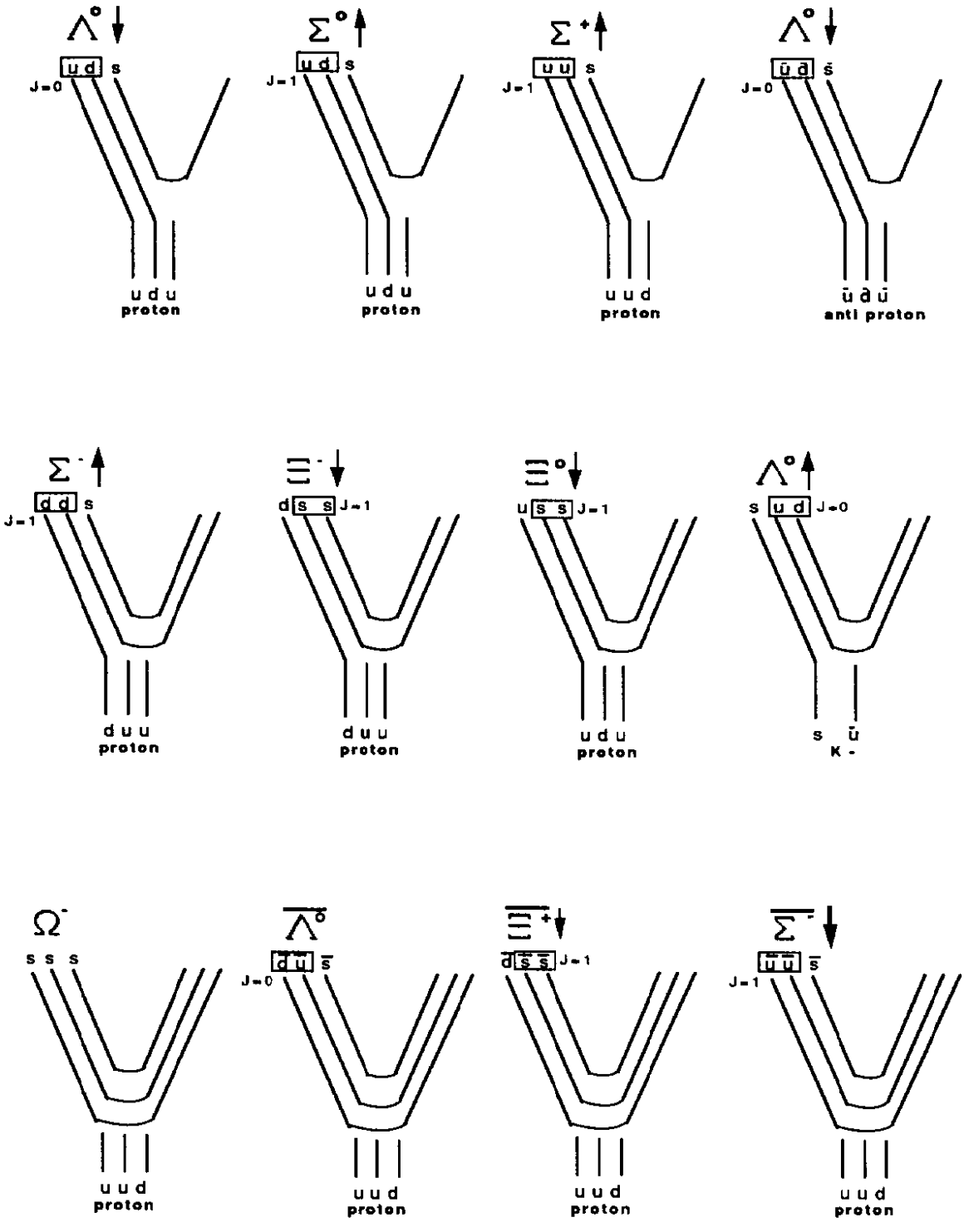

Figure 23. Hyperon Polarization Diagrams

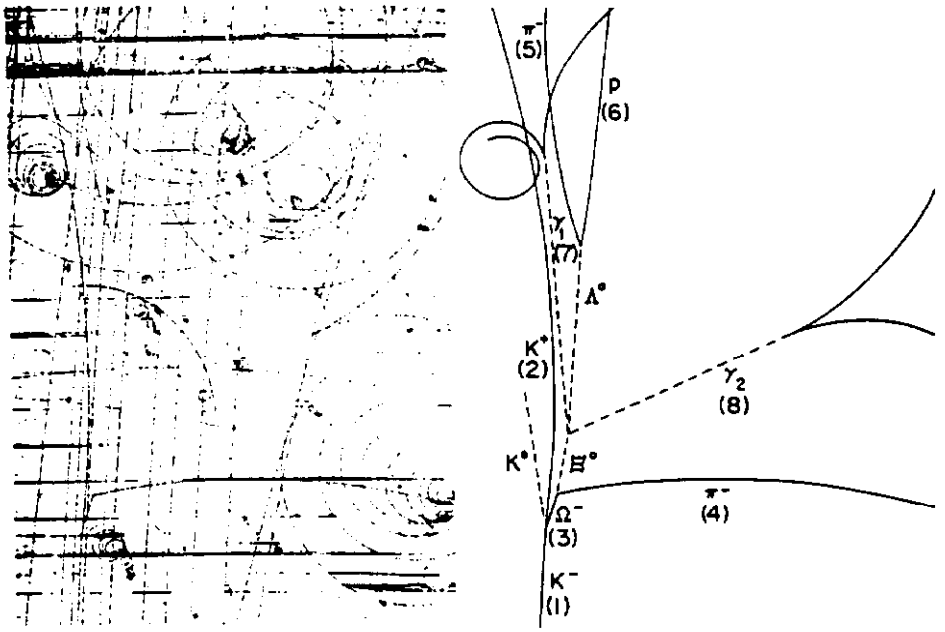

Figure 24. First Ω^- in the BNL 80" bubble chamber[31]

Figure 24 shows the first Ω^- event seen in the BNL 80 inch bubble chamber[31] in 1964. It is a complex event and the visible decay chain is extraordinary in its completeness. It is also a very lucky event in that one observes the conversion of both photons from the π° decay. Since the radiation length in hydrogen is 8.65 m, compared to the full length of the 80 inch (2.03 m) bubble chamber, converting both photons was indeed fortuitous. Although a tremendous effort was made to collect a large sample of Ω^- events, the largest bubble chamber sample, 101 events, was published[32] in 1978. This experiment showed that the spin of the Ω^- could not be 1/2, was consistent with a spin 3/2 assignment, but could not exclude a higher spin.

The CERN SPS hyperon beam was the first to produce large numbers of Ω^- events and obtained the first precise determination[33,8] of its lifetime with a sample of $\approx 13{,}000$ events. The Fermilab E756 group[34-36] now has event samples an order of magnitude larger.

In order to measure the magnetic moment by the classical spin precession technique one needs to produce a polarized sample of the particles of interest. How does one produce a polarized Ω^-? Clearly, when one starts with an incident proton beam, one must produce all the s quark constituents of the Ω^- from the sea. If hyperon polarization is a leading particle effect then the Ω^-, as the antihyperons, should not be polarized.

The first attempt by the E756 group to produce a polarized hyperon beam is shown as the Phase 1 configuration[35] in Figure 25. This is a plan and elevation view of their channel and targeting scheme. The angle of the beam incident on the target could be changed by a set of upstream magnetic elements. The results of running in this configuration are shown[34-35] in Figure 26. The disappointing result is that the polarization of the Ω^- is not significantly different from zero.

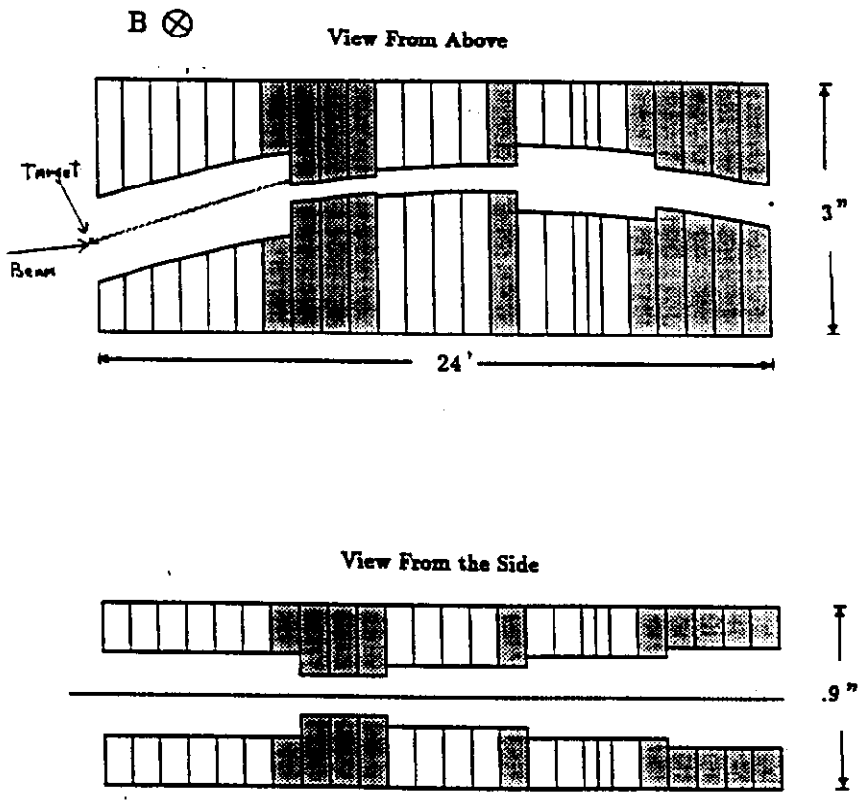

Figure 25. E756 Phase 1 configuration for measuring the Ω^- magnetic moment. The proton beam enters from the left. The channel is brass except the shaded region which is tungsten.

A modification of the E756 apparatus was made to produce the Ω^- as a tertiary beam. The idea was to use a beam of neutral polarized particles to produce the Ω^- and hope that the polarization of the neutral particles could be transferred to the Ω^-. The suggestion that there might be a significant spin transfer from a neutral polarized hyperon to the Ω^- was made by DeGrand et al.[37]

Figure 27 shows the primary target moved upstream and followed by a dipole which swept the produced charged particles away from the second target. Impinging on the second target are the neutral particles produced from the first target. This neutral beam is rich in $\Lambda^\circ, \Sigma^\circ$, and Ξ° which we know can be produced with significant polarization by changing the proton beam angle on the first target. Of course, the intensity on the second target is much less than in the Phase 1 configuration. Figure 28 shows the measured polarization of the Ω^- in the Phase 2 configuration. Although not extremely large, the polarization is sufficient to provide a measurement[36] of the Ω^- magnetic moment. This was the first demonstration of spin transfer in a hyperon beam.

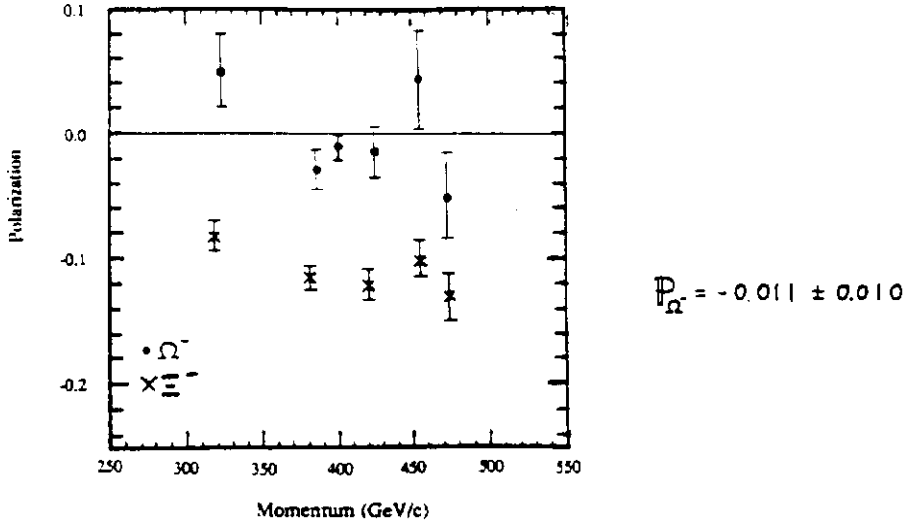

Figure 26. E756 Phase 1 results for the Ξ^- and Ω^- polarizations. Note that the Ω^- does not show any polarization.

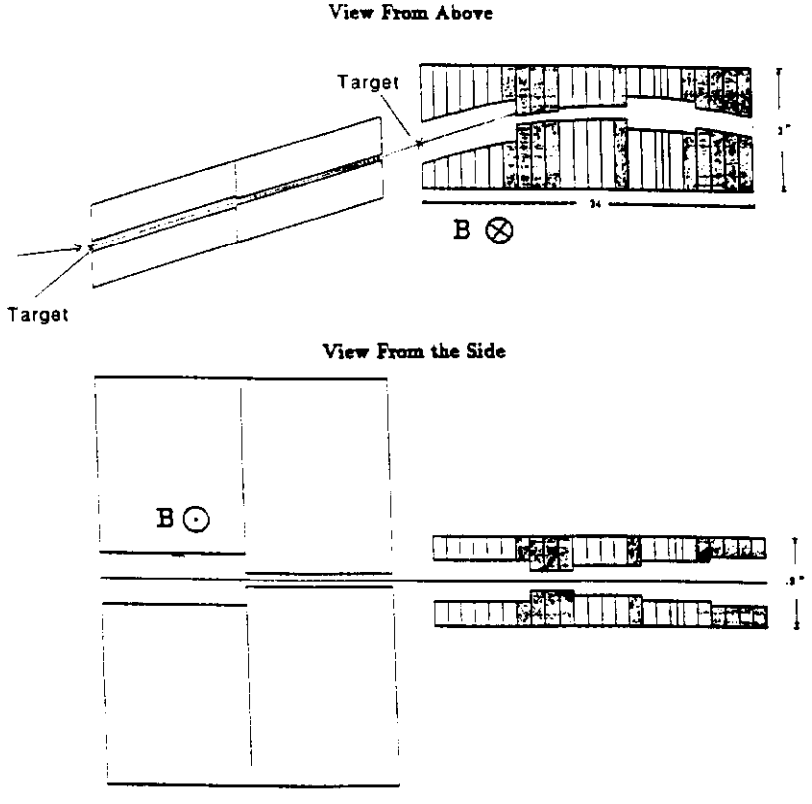

Figure 27. E756 Phase 2 configuration for measuring the Ω^- magnetic moment. Charged particles produced from the upstream target are swept by the added magnet. The remaining neutral particles which are polarized produce polarized Ω^- in the downstream target.

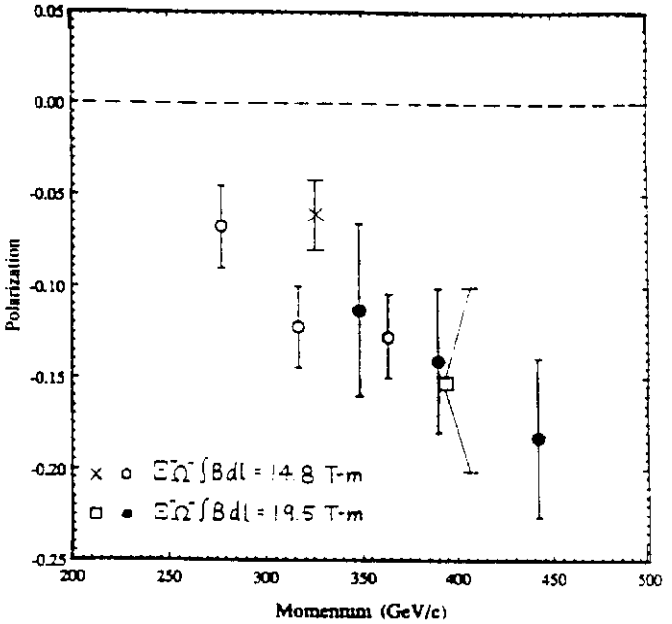

Figure 28. E756 Phase 2 results for the Ξ^- and Ω^- polarizations. Note that the Ω^- has significant polarization.

5. Baryon Magnetic Moments

The last ten years have seen great advances in the measurements of the baryon magnetic moments (Table 4). There now exist measurements of the magnetic moments of all the baryon octet shown in Figure 2 except for the Σ^0. That one has a lifetime too short for it to travel a significant distance, even at the highest energies now available. In the baryon decouplet a measurement now exists of the Ω^- magnetic moment.

Measurements of baryon magnetic moments have provided important insights into composition of baryons as well as useful constraints for model builders. These measurements show that a simple quark model describes most of the salient features. However, the significant discrepancies have raised fundamental questions about baryon structure and produced a steady stream of theoretical papers. I would like to briefly review the technology for making these measurements, the current state of the measurements, and the near term prospects for improvements. I will then comment on the comparisons with the quark model.

Magnetic Resonance Techniques. The magnetic moments of the proton and neutron are known to great accuracy.[38] Highly sensitive magnetic resonance techniques[39,40] allow measurement uncertainties of 0.022 ppm for the proton and 0.235 ppm for the neutron. These uncertainties are orders of magnitude smaller than those for the other baryons.

Exotic Atoms. A method that has been used to measure the antiproton[41] and the Σ^- hyperon[42] magnetic moments utilizes stopping a beam of these particles and forming an "exotic" atom. This "exotic" atom consists of a negative baryon captured near rest by a nucleus. X-rays from the exotic atom transitions are detected with high resolution solid state detectors. From the hyperfine splitting the hyperon magnetic moment can be inferred.

Table 4. Baryon Magnetic Moments

Baryon	Magnetic Moment μ_N	Quark Model μ_N	Difference μ_N	σ	%Dif
p	2.792847386 ± 0.000000063	input			
n	-1.91304275 ± 0.00000045	input			
Λ°	-0.613 ± 0.004	input			
Σ^+	2.419 ± 0.022	2.67	-0.251 ± 0.022	-11.41	-9.40
Σ^-	-1.156 ± 0.014	-1.09	-0.066 ± 0.014	-4.71	6.06
$\Sigma^\circ \rightarrow \Lambda^\circ$	-1.61 ± 0.08	-1.63	0.02 ± 0.08	0.25	-1.23
Ξ°	-1.253 ± 0.014	-1.43	0.177 ± 0.014	12.64	-12.38
Ξ^-	-0.675 ± 0.022	-0.49	-0.185 ± 0.022	-8.41	37.76
Ω^-	-1.94 ± 0.17	-1.84	-0.10 ± 0.17	-0.59	5.43

Complications occur because the captures are usually done in heavy elements. There are significant atomic physics corrections, and one is not able to resolve all the transition lines. This method has yielded a measurement of the Σ^- magnetic moment which is consistent with the somewhat more precise measurement[43] done by the classical spin precession technique. The weighted mean of these results is given in Table 4.

Primakoff Method. The electromagnetic decay, $\Sigma^\circ \rightarrow \Lambda^\circ \gamma$, is a magnetic dipole transition and has associated with it a transition magnetic moment. This transition moment is described by the same formalism as the static magnetic moments and amenable to the same quark model predictions. It has been measured[1] by the Primakoff[44] method.

Classical Spin Precession. The measurement of the spin precession in a magnetic field has been the most productive technique for yielding hyperon magnetic moments. Contributing to that success have been the following.

1. The advent of high momentum (hundreds of GeV/c) hyperon beams has allowed hyperon decay lengths of a few to tens of meters. Thus, hyperon path lengths sufficient to traverse significant magnetic fields are now at hand.
2. Short ($\approx$10 meters) beams with very significant hyperon fluxes have made possible high statistic measurements.
3. The hyperon parity violating weak decays allow an easy way of identifying the hyperon spin direction.
4. An unpolarized proton beam impinging on an unpolarized target can produce hyperon beams of significant polarization. Many (but unfortunately not all) hyperons have significant polarization (10-25%) at $p_t \approx 1$ GeV/c.

5. The discovery by Fermilab E756 that the Ω^- is not produced with any significant polarization led this group to use a double targeting technique to produce a polarized Ω^- beam.

Figure 29 illustrates the targeting geometry and baryon spin precession for the measurement of Λ° magnetic moment. This geometry has a vertical magnetic field (Y direction) and the Λ° polarization in the X direction. Since the incident proton beam is in the Y-Z plane (vertical targeting) the only polarization allowed in the parity conserving strong interaction is in the X plane. As the Λ° traverses the magnet the spin is precessed by an angle

$$\Phi \text{ (degrees)} = 18.3\ \mu_B/\beta\ \int B \cdot dl \text{ (T-m)}$$

where μ_B is the baryon magnetic moment in units of the proton nuclear magneton, $\mu_N = e\hbar/(2\ m_p c)$. Here m_p is the proton mass and β is the baryon velocity divided by the speed of light. If the targeting is done in the horizontal plane (beam in the X-Z plane), the allowed polarization would be in the vertical (Y) direction. Since it is now parallel to the magnetic field, there would be no spin precession. By changing the sign of the angle (Θ) one reverses the polarization of the hyperon beam. The ability to control the direction of polarization gives us an important tool for the control of systematic uncertainties.

Measurement[45] of the Λ° magnetic moment using the targeting geometry of Figure 29 and the detector geometry of Figure 12 yielded an extremely precise Λ° magnetic moment, $\mu_\Lambda = -0.6138 \pm 0.0047 \mu_N$. This is less than a 1% uncertainty of the magnetic moment! Figure 30 shows the spin precession as a function of the field integral. Measurements[46] of the Ξ° magnetic moment have been done with a similar apparatus.

It is somewhat easier to control systematic uncertainties in magnetic moment measurements for neutral hyperons as illustrated in this figure. For a charged hyperon this is complicated by the fact that the hyperon momentum changes with the magnetic field.

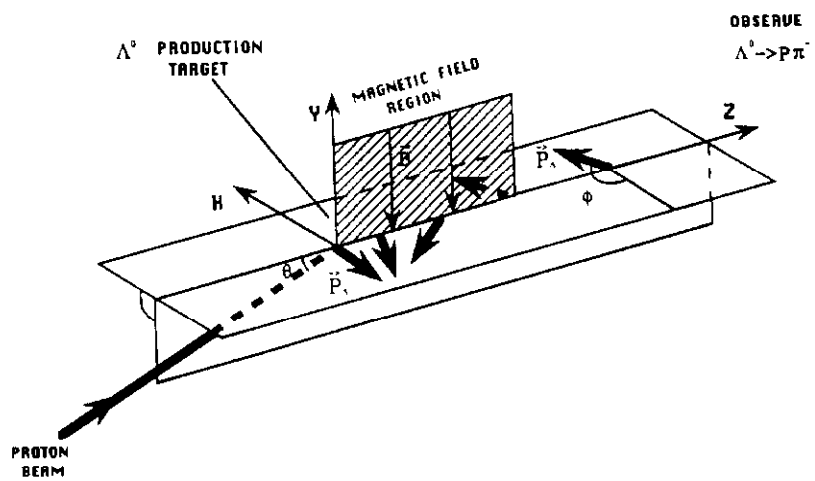

Figure 29. Beam targeting geometry and spin precession of a Λ° hyperon

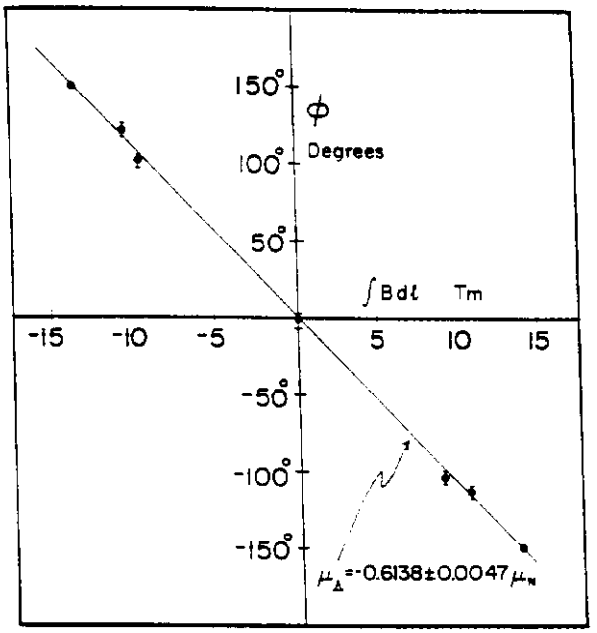

Figure 30. Λ° spin precession angle as a function of field integral

Referring back to Figure 6, we can write the spin rotation, relative to the baryons' direction of motion, as it traverses a magnetic field

$$\Phi \text{ (degrees)} = 18.3\ (g/2-1)\ (m_p/m_B)\ /\beta \int B \cdot dl \text{ (T-m)}.$$

We write μ_B in terms of the g-factor and the spin vector.

$$\mu_B = g/2\ (e/m_B)S$$

For the Fermilab Proton Center hyperon beam, typical values of these parameters are magnetic field, B=3.5 T and length, l= 7 m. For a 350 GeV/c Σ^+ these yield a spin rotation $\Phi \approx 700°$. This is not a small effect!

I will now review the status of some recent measurements of the charged baryons' magnetic moments. I have tabulated the magnetic moment values starting with the initial operation of the Fermilab hyperon beams. I apologize to the authors of earlier measurements that I will not mention; however, the data is really dominated by results from the start of this period. I will not spend much time on the neutral hyperon measurements since the 1985 review article of Pondrom[6] is still a good description.

The Σ^+ magnetic moment. The agreement is poor between measurements from two Fermilab experiments[47,48] shown in Figure 31. These two, nominally 1% measurements differ by 3.1σ, indicating one or both of them probably have errors larger than stated. This is a well known problem and has been handled by increasing the error of their mean to $2.419\pm0.022\mu_N$. Although not crucial for the confrontation of existing models, it may soon be tidied up. Fermilab E761 has repeated this measurement with apparatus of considerably

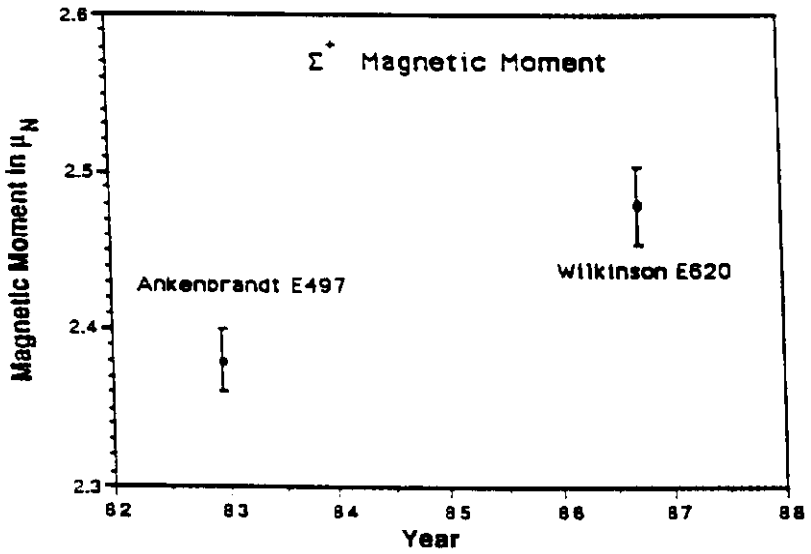

Figure 31. Σ^+ Magnet Moment Status

better angular and momentum resolution. They have also collected an order of magnitude more data. Hopefully, we will soon see a resolution to this discrepancy.

The Σ^- magnetic moment. Figure 32 shows the recent history of Σ^- magnetic moment measurements.[42,43] The one with the highest precision[43] represents a combination of measurements at two beam momenta and two final states ($\Sigma^- \rightarrow n\pi^-$ and

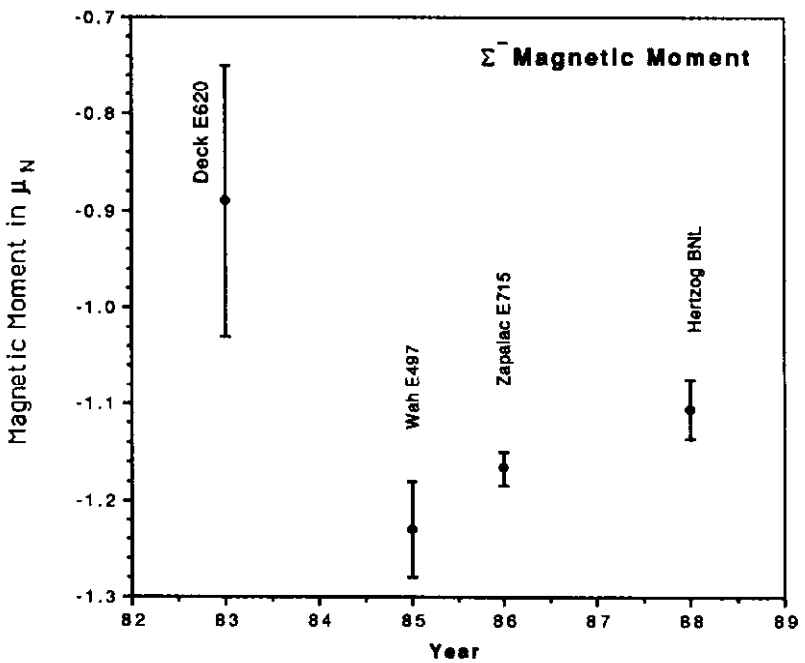

Figure 32. Σ^- Magnet Moment Status

$\Sigma^- \to n e^- \bar{\nu}$). Figure 33 shows a plan view of the apparatus from this experiment,[43] Fermilab E715. The major thrust was to measure the asymmetry parameter, α_e, in Σ^- β-decay. It was fortunate that α_e was sufficiently large to provide an excellent magnetic moment measurement even though this is a rare decay (Table 3). Figure 33 shows a typical particle trajectory for the decay $\Sigma^- \to n e^- \bar{\nu}$. A key ingredient was the double identification of the electron by both a TRD detector and a lead glass array. In decays of $\Sigma^- \to n\pi^-$, the pion distributions are similar to the electron so the same experimental configuration was used.

The final value from the exotic atom measurement[42] differs from the E715 measurements by 1.7σ, the agreement being reasonable. The weighted mean (Table 4) of these measurements yields a Σ^- magnetic moment of -1.156±0.014μ_N.

The Ξ^- and $\bar{\Xi}^+$ system. Recent results from Fermilab E756 have yielded a new value of the Ξ^- magnetic moment[34,35] and the first measurement of the $\bar{\Xi}^+$ magnetic moment.[23] Displayed in Figure 34 are measurements of the Ξ^- magnetic moment from three Fermilab experiments.[34,35,49,50] The result quoted in the thesis of H. Diehl[35] has a very small error, μ_Ξ = -0.650 ±0.005 ±0.002 μ_N; the uncertainties are statistical andsystematical, respectively. However, a result presented by K. B. Luk[34] from the same experiment has a considerably larger uncertainty, μ_Ξ = -0.674 ±0.021 ±0.020 μ_N. It is preliminary and from a partial data sample. At this time it appears the E756 experimenters are not totally at ease with the Diehl result. In my composite result in Table 4, I use the Luk number. Hopefully, the Diehl number is representative of the final uncertainty that we may expect from this experiment.

Figure 35 shows the E756 apparatus that had as its prime goal the measurement of the Ω^- magnetic moment. It also made important measurements of the the Ξ^- and $\bar{\Xi}^+$ moments since these topologies are similar.

Symmetry under the combined operation of charge conjugation, parity inversion, and time reversal (CPT) requires that magnetic moments of particle and antiparticle be identical in magnitude but opposite in sign.

The data of Ho et al.[23] is a matched set of both the Ξ^- and $\bar{\Xi}^+$ magnetic moments. They find for the $\bar{\Xi}^+$ a value of 0.657 ±0.028 ±0.020 μ_N; the matching measurement for the Ξ^- yields -0.674 ±0.021μ_N. As expected, the two measurements are in good agreement with the prediction of the CPT theorem.

Also, Fermilab E761 finds their sample of $\bar{\Sigma}^-$ polarized and should be able to extract a magnetic moment. For completion we note that there is good agreement[1] between the magnitude of the antiproton magnetic moment (-2.795±0.019 μ_N) and the proton moment (2.793 μ_N).

The Ω^- measurements. A recent final result[36] of the Ω^- magnetic moment from E756 is included in the Table 4 summary: $\mu_\Omega = -1.94 \pm 0.17 \mu_N$. This experiment will run again in 1991 as Fermilab E800 and expects to produce a measurement with a precision of ±0.03μ_N.

Comments On Magnetic Moments. I would like to put into perspective our knowledge of the baryon magnetic moments. Let us look first at the electron and muon magnetic moments. Both of these have been measured extremely well[38] in comparison

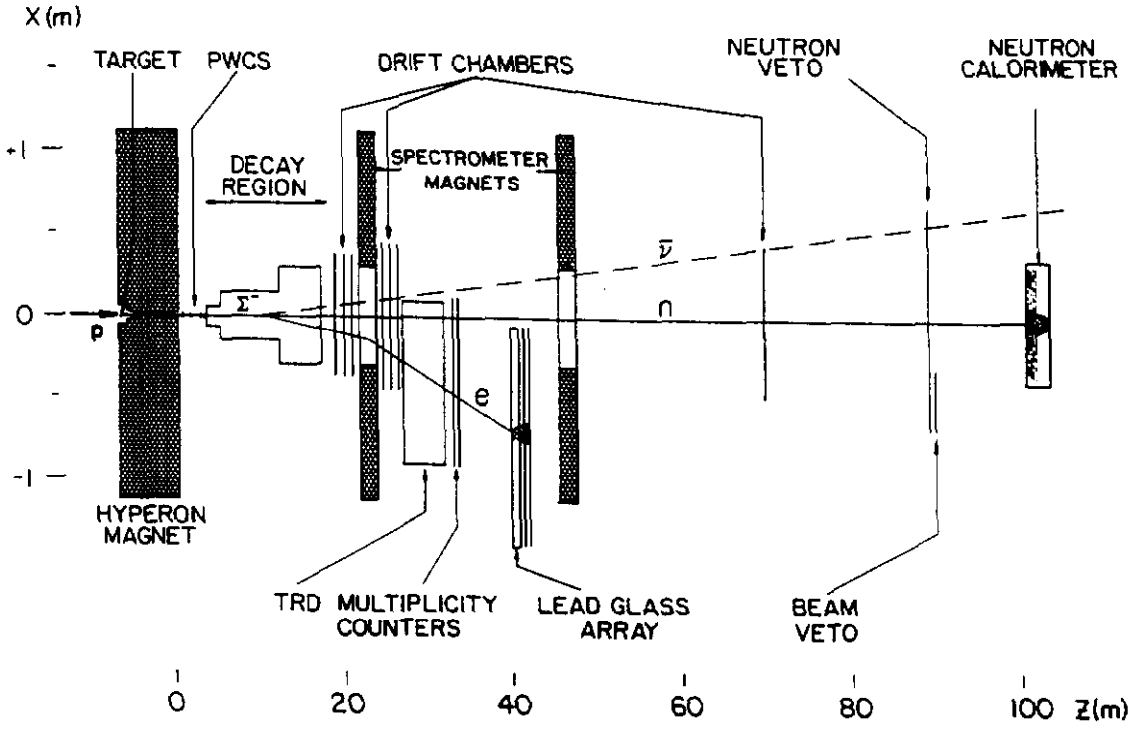

Figure 33. Plan view of Fermilab E715 apparatus. Note the double identification of the electron.

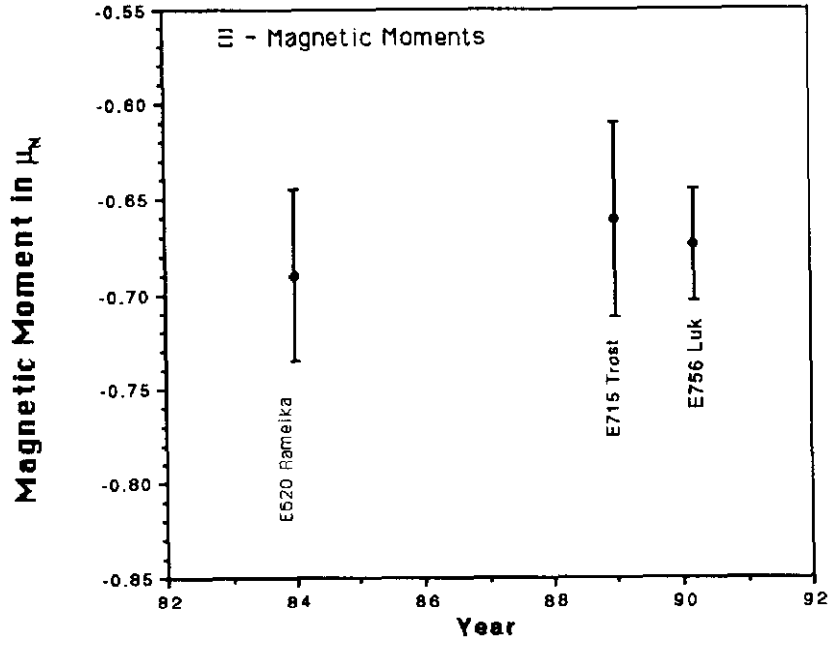

Figure 34. Ξ^- Magnetic Moment Status

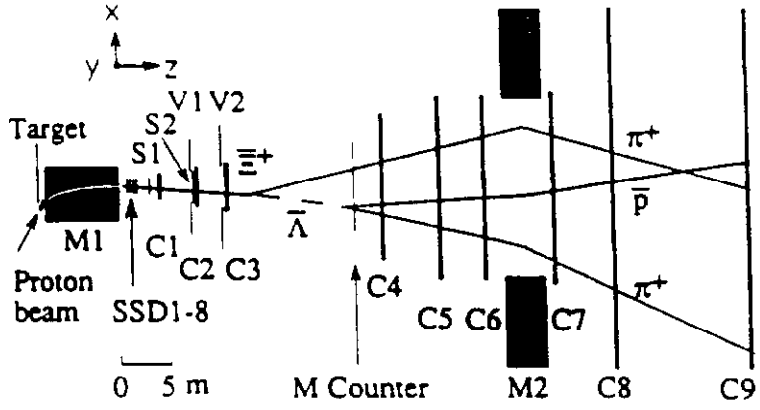

Figure 35. Plan view of Fermilab E756 apparatus

with the baryons. I choose to quote not their magnetic moments, but one half their g-factors. For a simple Dirac particle this should be one.

Electron	g/2 =	1.001 159 652 00 (40)	experiment
		1.001 159 652 570 (150)	theory
Muon	g/2=	1.001 165 924 (9)	experiment
		1.001 165 921 (8)	theory

Listed first is the experimental value and then the prediction of theory.[51] In parentheses is the estimated uncertainty of each. The deviation from unity is due to higher order strong and electromagnetic corrections which can be computed. Note that the agreement here is very satisfying.

The proton and neutron precision measurements[1] have been available for a long time. However, it was not until the advent of the quark model that we had a method of evaluating them. Let me illustrate by writing

$$\mu_p = 2.792\ 845\ 6\ (11)\ \mu_N$$
$$\mu_n = -1.913\ 041\ 84\ (88)\ \mu_N$$

Even though the proton and neutron are Dirac particles they certainly do not have simple Dirac moments. Before the quark model this discrepancy was attributed to structure due to their strong interactions. This was the original reason for postulating the ω and ρ mesons.

With the quark model we can write the magnetic moments of the baryons (μ_B) as sums of the moments of their constituents.

$$\mu_B = \sum \langle B | \mu_i | B \rangle \quad \text{where } \mu_i = e_i \hbar/(2m_i e)$$

and e_i are the quark charges. We can use our quark wave functions of Figure 22 to compute the moments. Assuming the equality of the u and d quark masses we can calculate the ratio

$$\mu_n/\mu_p = -2/3$$

Experimentally this number is

$$\mu_n/\mu_p = -0.684\ 979\ 75\ (58)$$

Although this was viewed as a success for the quark model, a skeptical experimentalist would note that it differed by $\approx \pi \cdot 10^4$ standard deviations!

Measurements of the hyperon moments allow for a much wider test of the quark model. I write the baryon magnetic moments in terms of their quark constituents.

$$\begin{aligned}
\mu_p &= 4/3\ \mu_u - 1/3\ \mu_d \\
\mu_n &= 4/3\ \mu_d - 1/3\ \mu_u \\
\mu_\Lambda &= \mu_s \\
\mu_{\Sigma^+} &= 4/3\ \mu_u - 1/3\ \mu_s \\
\mu_{\Sigma^-} &= 4/3\ \mu_d - 1/3\ \mu_s \\
\mu_{\Xi^0} &= 4/3\ \mu_s - 1/3\ \mu_u \\
\mu_{\Xi^-} &= 4/3\ \mu_s - 1/3\ \mu_d \\
\mu_{\Sigma^0\to\Lambda} &= (1/\sqrt{3})(\mu_d - \mu_u) \\
\mu_{\Omega^-} &= 3\mu_s\ .
\end{aligned}$$

I have included the transition moment for the $\Sigma^0 \to \Lambda^0\ \gamma$ electromagnetic decay[52] that was discussed earlier under the Primakoff method.[44]

Although the Ω^- is not a member of the octet, the assumption that it is composed of three aligned s quarks allows a magnetic moment prediction. We have nine relations among three unknown parameters, the quark magnetic moments.

The three most precisely measured baryon moments, p, n, and Λ^0, serve as input parameters for the prediction of the rest. Table 4 summarizes the current status of the baryon magnetic moments. The sign of the $\Sigma^0 \to \Lambda^0$ transition moment is taken from the quark model. Table 4 also shows the differences from the moments predicted by the quark model. Figure 36 is a plot of the differences. Here the error on the Λ^0 moment is plotted to illustrate the precision of the Λ^0 compared to the others. The larger errors on the $\Sigma^0 \to \Lambda^0$ transition moment and the Ω^- moment distinguish them from the rest.

The quark model predictions reproduce all the signs correctly. In magnitude the worst disagreement is about 0.25 μ_N. This agreement makes you feel you are on the right track. However, this is far from the complete story as a glance at the columns showing the deviation in σ and in % difference will attest. The Ξ^-, with a $\approx$30% deviation, is striking.

In the near future one can hope for some improvement in these measurements. E761 should be able to help resolve the discrepancy between the two existing measurements of

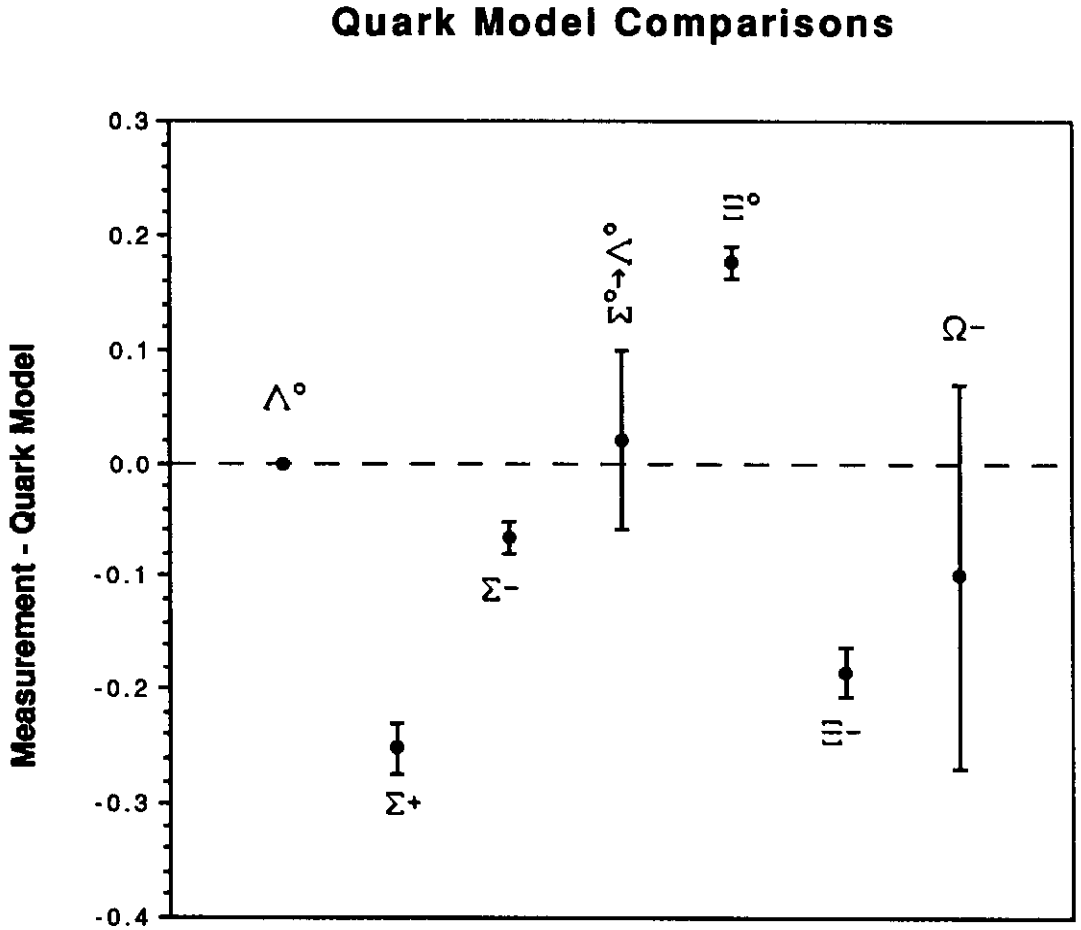

Figure 36. Comparisons of the baryon magnetic moments with the quark model

the Σ^+ moment. E756 has data which should allow it to improve the Ξ^- moment, and with the expected running of E800 this summer we may expect a substantial improvement in the Ω^-.

The simple quark model comparison is clearly just the initial step in making comparisons with theory; many more embellishments have been made. What are the effects of gluon currents, the quark sea, relativistics effects, admixtures of orbital configurations in the baryon wave functions? There is too large a volume of literature on this topic to go into detail here. I recommend the list of theory references on page VIII.62 of reference 1.

The baryon magnetic moments will continue to be a challenge to theorists. Models will at least have to give passing reference to the agreement (or lack thereof) of these increasingly more precise measurements. Referring to Table 4, I alternate between being impressed that such a simple picture gives good general qualitatative agreement with the measurements and depressed when I compare them to the agreement we have with the magnetic moments of the electron and muon.

Crystal channeling. The phenomenon of crystal channeling[53] has been of interest because of the very high effective magnetic fields that are involved. Figure 37 illustrates this phenomenon. Figure 37a depicts a crystal oriented so that a charged beam enters almost

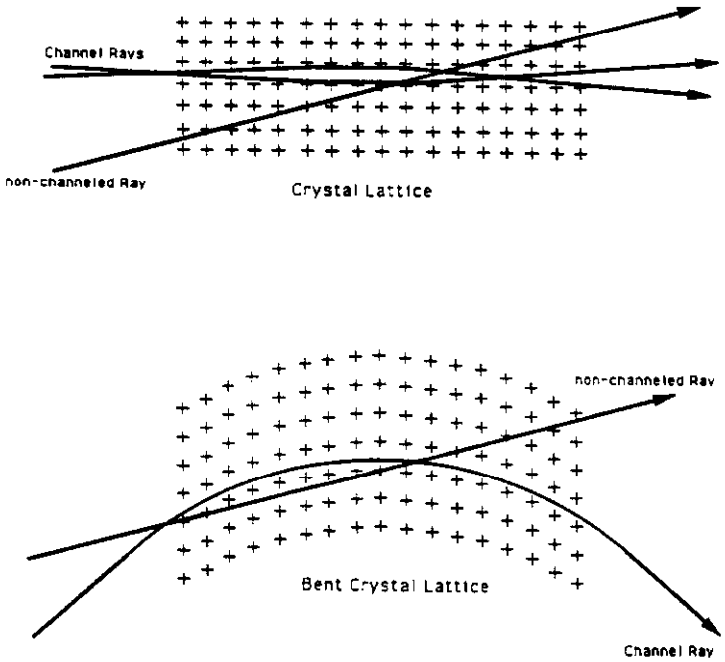

Figure 37. Channeling in straight and bent crystal

parallel to the crystal axis. A positively charged particle entering thus finds itself in a potential well formed by the positively charged arrays of nuclei. It is trapped -channeled- in this potential if the incident angle is near the crystal plane. If the angle is too large it passes through the crystal without being channeled as indicated in the same figure.

If one now bends the crystal as depicted in Figure 37b, one finds that one also bends the channeled beam.[53] From the momentum of the particle and the bend angle one realizes that the effective magnetic fields inside the crystal can be very large. Can these same large fields be used to precess the spin direction of a polarized beam? Fermilab E761, whose main goal was to look at hyperon radiative decays ($\Sigma^+ \to p\gamma$ and $\Xi^- \to \Sigma^-\gamma$), attempted to see this effect in a subsidiary experiment. A beam containing Σ^+ hyperons is a good candidate for investigating this effect since they can be produced polarized and have a large decay asymmetry parameter ($\alpha = -0.98$) for the common decay mode, $\Sigma^+ \to p\pi^\circ$. Hence, one can readily measure their spin direction from the decay distribution.

Figure 38 schematically shows the crystal configuration used in E761. A single crystal of silicon was placed in a 375 GeV/c beam which contained about 1% Σ^+ (the rest being mainly protons and π^+). This crystal was also implanted with eight solid state energy loss detectors so that the energy deposited in the crystal could be measured for each incident particle. Apparatus upstream (not shown) of the crystal measured the incident particle momentum and angle (with a precision of $\approx 0.2\%$ and ≈ 10 μrad respectively). A downstream spectrometer (also not shown) measured the particle momentum and trajectory a second time. Figure 39 shows some preliminary results where no distinction is made between particle types. Thus it contains mostly protons and π^+. Figure 39a shows the

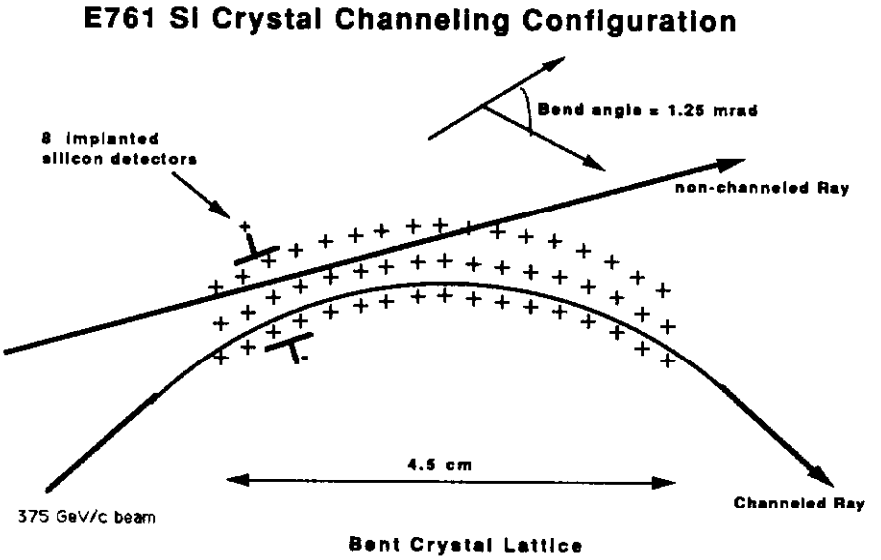

Figure 38. Crystal setup for channeling

difference between the angle measured entering and exiting the crystal. One sees a peak at about 1.25 mrad which is the known bending angle of the crystal.

Another characteristic is that the channeled particles lose less energy due to ionization than their non-channeled counterparts. This is seen in Figure 39b and 39c which shows the energy deposition in the crystal aligned with the beam (so some beam will be channeled) and the energy loss for the same crystal not aligned with the beam (so there will be no channeling). One sees a clear signal of a smaller energy loss in the aligned case.

The crystal bend angle of 1.25 mrad corresponds to an effective magnetic field of ≈ 35 T within the crystal. With the known Σ^+ magnetic moment one would expect a spin rotation of $\approx 42.5°$ in the crystal. About 5000 Σ^+ events have been recorded and assuming a beam polarization of 15%, this should lead to a measurement of the rotation angle to a precision of $\approx 12.5°$ which should be enough to see the effect. We look forward to the results from this data.

The crystal bend angle of 1.25 mrad was chosen to match the acceptance of the downstream spectrometer. The crystal was bent to angles as large as 10 mrad (without breaking!) which would correspond to an effective magnetic field of 275 T.

In the longer range one might consider applying this technique to charmed baryons which have a much shorter lifetime[1] than Σ^+. Note that at 500 GeV/c the Λ_c^+ and Ξ_c^+ would have decay lengths of 1.18 and 2.64 cm respectively.

6. Hyperon Radiative Decays

Radiative decays of hyperons are a class of reactions which are simple in their kinematics: just the decay of one baryon into another with the emission of a photon. Yet they are also complicated in that they probe the interplay of the electromagnetic, weak, and strong interactions.

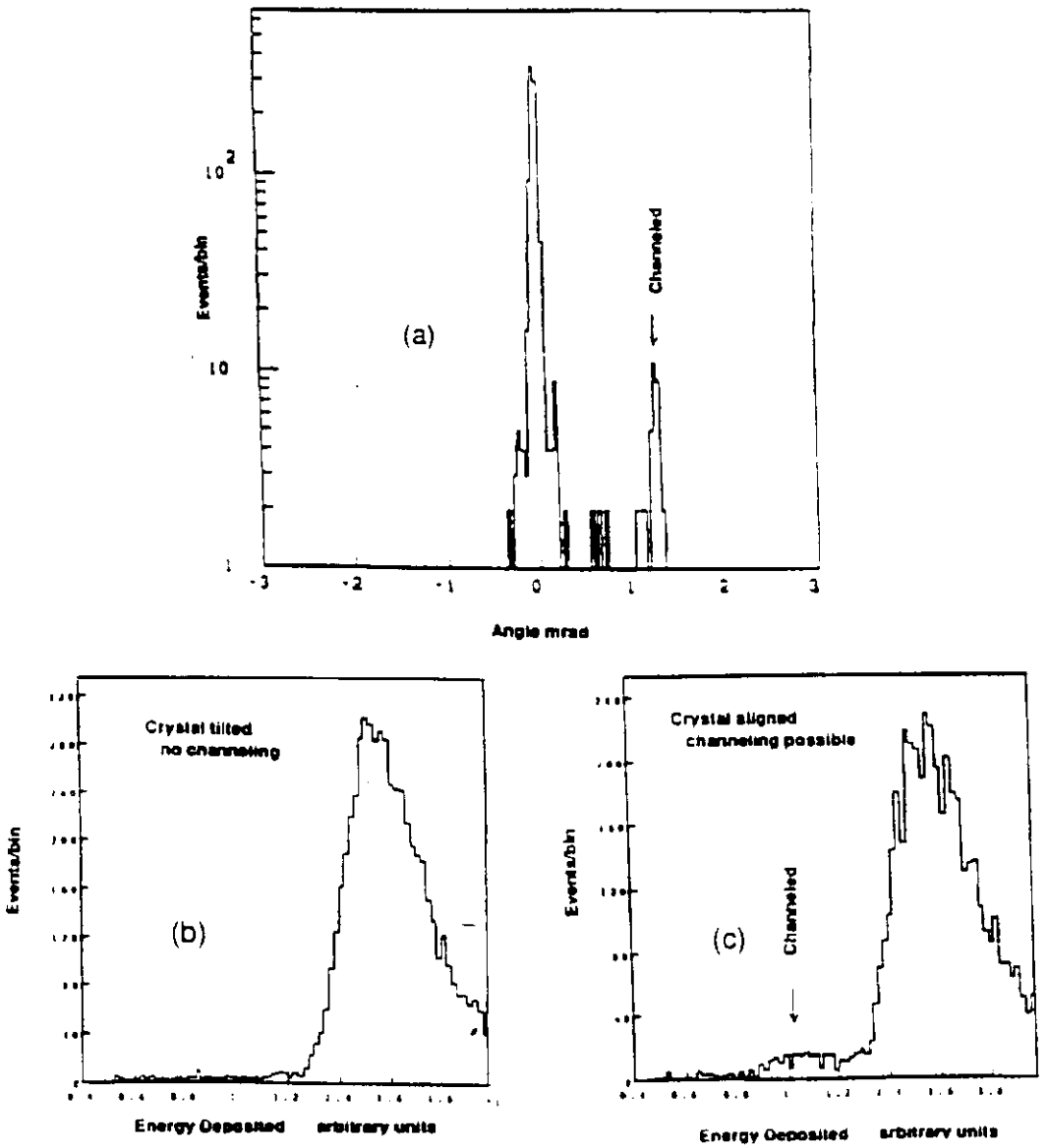

Figure 39. Crystal Channeling Data. (a) Deflection of beam by crystal. (b) Energy loss for non-channeled particles. (c) Energy loss for all particles showing showing low energy loss for channel component.

Let us illustrate with the simplest of these reactions: $\Sigma^+ \to p\gamma$. Our previous example, Figure 3, shows such a decay. Here a beam of 390 MeV/c K^- mesons is used to produce Σ^+ in a 25 inch diameter hydrogen bubble chamber.[2] The short heavily ionizing track is the Σ^+, which in this rare photograph decays to a $p\gamma$. Electromagnetic processes are clearly important since a photon is involved. The decay is a weak process since the baryon strangeness changes. Finally, the strong force must also be involved since it provides the fundamental distinction between the proton and Σ^+.

What can we measure? We can measure the branching ratio; that is, the probability that a Σ^+ will decay to a $p\gamma$ compared to the other allowed decays. A series of early experiments with very limited statistics indicates this branching fraction is small, $\approx 1 \times$

10^{-3}. Even more challenging for the experimenter is that a major decay mode is $\Sigma^+ \to p\pi^\circ$ with the subsequent decay, $\pi^\circ \to \gamma\gamma$, providing a confusing background.

Of the radiative decays, $\Sigma^+ \to p\gamma$ has been studied most from both an experimental and theoretical point of view. Table 5 summarizes the meager experimental data on this and the other radiative decays.

More information may be gleaned from the decay if the Σ^+ is polarized and one measures the correlation of the direction of proton emission to the direction of the Σ^+ polarization. In the rest frame of a polarized $\Sigma^+ \to p\gamma$ the angular distribution of the decay proton is given by

$$dN/d\Omega \approx 1 + \alpha_\gamma P_\Sigma \cos\theta$$

where α_γ is the asymmetry parameter of interest, P_f is the polarization of the Σ^+, Ω is the solid angle, and θ is the angle between the proton momentum and the Σ^+ polarization direction.

Hara[54] showed in 1964 that in the standard current-current form of the weak interaction, with no CP violation, **AND** in the SU(3) limit, $\alpha_\gamma \to 0$. In a simple calculation of first order symmetry breaking α_γ would tend to become positive for the Σ^+ decay. Hyperon radiative decays have been analyzed theoretically using single quark transitions, internal W exchange, penguin diagrams, long distance effects, and QCD sum rules.[55-62] Some of the contributing diagrams are shown in Figure 40.

The first two can contribute to all of the radiative decays; the last diagram cannot contribute to $\Xi^- \to \Sigma^-\gamma$ or $\Omega^- \to \Xi^-\gamma$ since neither of the initial hyperons contain a valence u quark. The one quark transition diagram predicts amplitudes much smaller than those observed. To quote from Kogan and Shifman,[55] "The mechanism of this diagram cannot play an important role in weak radiative decays".

Hara's Theorem and the simplest models predict α_γ to be zero. However, the early experiments, as seen in Table 5, with statistics of only a few hundred events indicated that α_γ was large and negative. These results confounded theorists and worried some experimenters since it might be explained by an unexpected contamination of the $\Sigma^+ \to p\gamma$ events with an unresolved background from much more copious $\Sigma^+ \to p\pi^\circ$ decays which have a large negative asymmetry.[1]

The Fermilab E761 collaboration was formed to conduct a definitive experiment on the radiative decay $\Sigma^+ \to p\gamma$. The apparatus constructed utilizes the Fermilab Proton Center hyperon beam which produces Σ^+ at ≈ 375 GeV/c. Because the Σ^+ particles are produced with large energies, they travel ≈ 8 m from their origin before they decay; hence, they are well separated from the clutter of their production region. The beam is polarized and, even more importantly, the direction of the Σ^+ polarization can be easily reversed, providing control of potential systematic errors.

A schematic view of the experiment is shown in Figure 41. It consists of 3 spectrometers, one for each of the particles in the decay $\Sigma^+ \to p\gamma$: a hyperon, a baryon, and a photon spectrometer. The hyperon spectrometer measures the Σ^+ momentum to 0.7%. It is composed of three stations (9 planes) of silicon strip detectors (SSD) and a magnet. The baryon spectrometer measures the proton momentum to 0.2%. It has four stations of

Table 5
A Summary Hyperon Radiative Decay Data

	Branching Ratio	α	Events	
$\Sigma^+ \to p\gamma$	$1.16 \pm 0.21 \times 10^{-3}$	-0.72 ± 0.29	≈ 107	Hydrogen Bubble Chamber data
	$1.27 \pm 0.17 \times 10^{-3}$		155	CERN, Biagi 1985
	$1.30 \pm 0.15 \times 10^{-3}$	$-0.86 \pm 0.13 \pm 0.04$	≈ 190	Kobayashi, 1987
	$1.45 \pm 0.30 \times 10^{-3}$		408	Hessey, 1989
$\Xi^- \to \Sigma^- \gamma$	$2.3 \pm 1.0 \times 10^{-4}$		11	CERN Biagi 1987
$\Xi^\circ \to \Lambda\gamma$	$1.06 \pm 0.16 \times 10^{-3}$	0.43 ± 0.44	116	James, Fermilab E619
$\Xi^\circ \to \Sigma^\circ \gamma$	$3.56 \pm 0.43 \times 10^{-3}$	0.20 ± 0.32	85	Teige, Fermilab E619
$\Lambda \to n\gamma$	$1.02 \pm 0.33 \times 10^{-3}$		31	CERN, Biagi 1986
$\Omega^- \to \Xi^- \gamma$	$< 2.2 \times 10^{-3}$			Bourquin, 1984

Hydrogen Bubble Data from Particle Data Group, Phys. Lett. 239 (1990).
Biagi et al., A Measurement of the BR $\Sigma^+ \to p\gamma / \Sigma^+ \to p\pi^\circ$, Z. Phys C28 (1985) 495.
Biagi et al., First Measurement of the $\Lambda \to n\gamma$ BR, Z. Phys. C30 (1986) 201.
Biagi et al., First Measurement of the $\Xi^- \to \Sigma^- \gamma$ BR, Z. Phys. C35 (1987) 143.
Kobayashi et al., New Measurement of the Asymmetry Parameter For the $\Sigma^+ \to p\gamma$ Decay. Phys Rev Letters 59 (1987) 868.
Hessey, et al., A Measurement of the $\Sigma^+ \to p\gamma$ BR. Z. Phys. C42 (1989) 175.
C. James et al., Phys Rev Lett 64 (1990) 843.
S. Teige et al., Phys Rev Lett 63 (1989) 2717.
M. Bourquin et al., Nucl Phys B241 (1984) 1.

proportional wire chambers (PWC) containing a total of 30 planes, and three magnets. The angular resolution of both the hyperon and baryon spectrometers is $\approx 10 \mu rad$.

Crucial to the separation of the single photon events from the π° background is the photon spectrometer, which measures the photon position and energy. It measures the photon position by converting the photon in two one-inch-thick iron plates. The high energy charged component of the produced shower follows closely the original photon direction. Transition radiation detectors (TRD) measure the center of the high energy electromagnetic shower. Wire chambers are used to supplement the TRD.

Measurement of the photon energy is done by a 112 element calorimeter. Most of the calorimeter is composed of lead glass; however, the central region is instrumented with 16 crystals of Bismuth Germanate (BGO). The BGO has a much shorter radiation length (about 1 cm) than lead glass and is capable of better photon position resolution.

An 800 GeV/c proton beam impinges on the Cu target at a finite targeting angle of ± 4 mrad in the horizontal, producing a 375 GeV/c polarized hyperon beam. The polarization is along the direction given by the cross product of the incident proton momentum and the outgoing Σ^+ momentum. We can reverse the targeting angle and thus reverse the polarization direction. This gives two sets of data, spin up and spin down, and allows

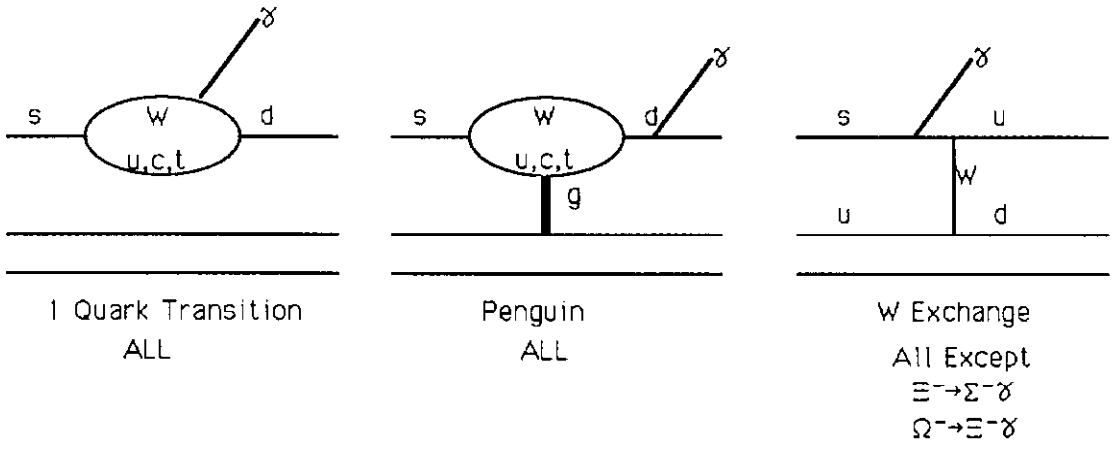

Figure 40. Relevant diagrams to radiative decays

cancelling biases in the apparatus by averaging over them.

We define the asymmetry, A, for a sample of Σ^+ decays as $A \equiv \alpha P_\Sigma$ where α is the asymmetry parameter for the specific decay and P_Σ is the hyperon polarization. We then measure the asymmetry for two different decay modes (A_γ for $\Sigma^+ \to p\gamma$, and A_0 for $\Sigma^+ \to p\pi^0$) with the same beam and hence the same P_Σ.

$$\alpha\gamma = (A_\gamma / A_0)\, \alpha_0$$

A_γ and A_0 are determined from the data sample and using the known[1] value of α_0 (-0.980 $\pm$ 0.016) can be inserted to determine α_γ.

Shown in Figure 42 is the missing mass squared distribution from their full data sample assuming the decay $\Sigma^+ \to p + X$. The size of the sample is such that it approaches 1 million events per bin! After making geometrical and kinematic selections, we find a value for $A_0 = -0.11$.

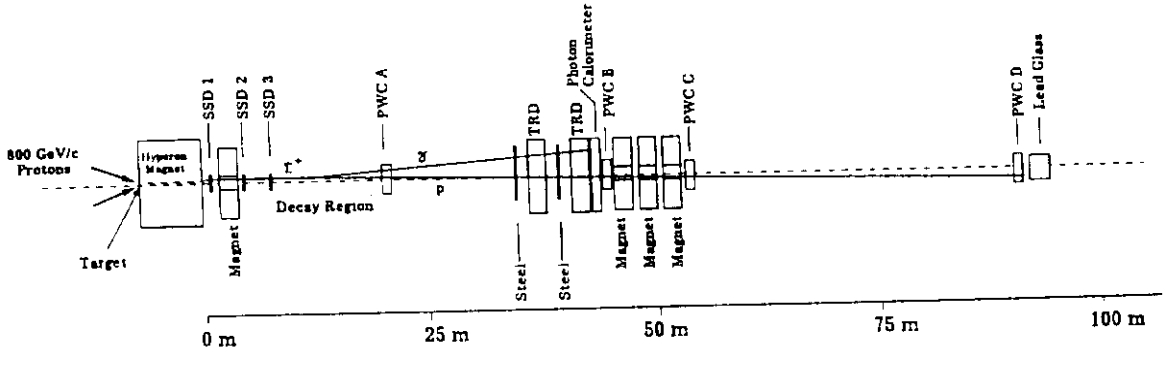

Figure 41. A plan view of E761 installed in Proton Center

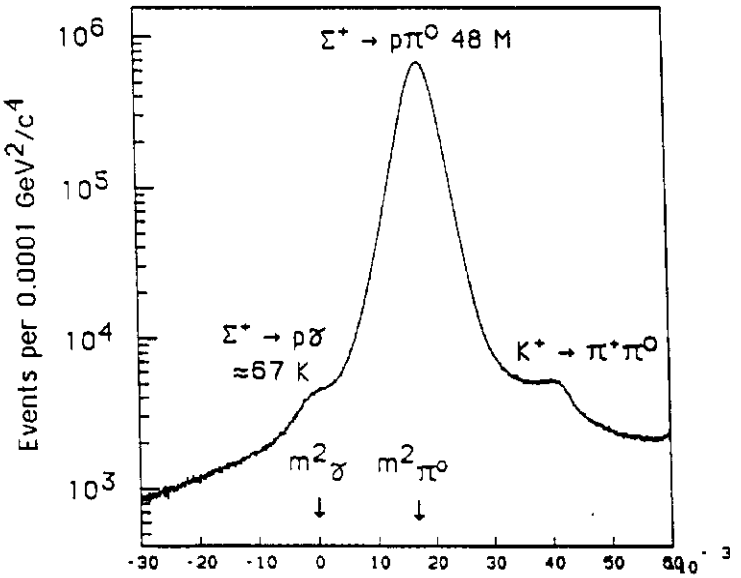

Figure 42. Missing mass squared distribution assuming the decay $\Sigma^+ \rightarrow p+X$. Minimum selection criteria imposed on data sample

From Figure 42 it is clear that the dominant background is $\Sigma^+ \rightarrow p\pi^\circ$. How do we separate $\Sigma^+ \rightarrow p\gamma$ from $\Sigma^+ \rightarrow p\pi^\circ$? We now use the photon position information from the TRD and photon energy measurements from the BGO and lead glass calorimeter. Shown in Figure 43 is the missing mass squared distribution with these restrictions. A clear peak is seen at the mass squared of the photon.

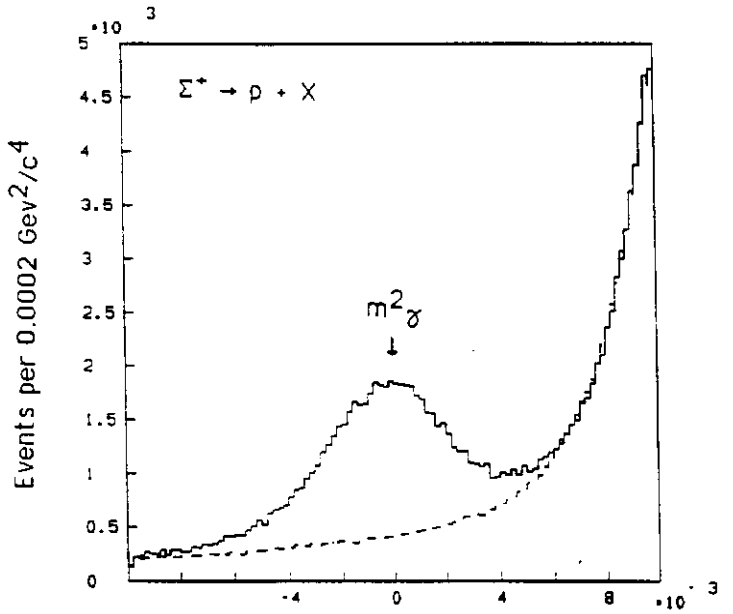

Figure 43. Missing mass squared distribution assuming the decay $\Sigma^+ \rightarrow p+X$. TRD and calorimetric selection of single photon events imposed.

Thus, we find $A_\gamma = -0.079 \pm .012$, which yields a value for $\alpha_\gamma = -0.69 \pm (0.11$ statistical) $\pm (0.11 \pm 0.11$ systematic). This is based on 37,816 $\pm$ 261 events and is a preliminary result[63] since systematic studies have not been completed. If one is optimistic, the systematic uncertainty might be reduced to where it is negligible, and if the statistics of the sample were fully exploited the combined error could be reduced to ± 0.07. The result agrees well with the previous lower statistics experiments in Table 5 and is also in agreement with the calculations of I. I. Balitsky, V. M. Brawn, and A. V. Kolesnichenko.[57]

The same experiment has also collected data on the decay $\Xi^- \to \Sigma^- \gamma$ and we look forward to seeing that result. Note that the W exchange diagram of Figure 40 cannot contribute to this decay.

7. Future Prospects.

I have tried to give a broad description of the development of hyperon beams and some of the physics they have done. The direction for future devolopments follows the lead of the final run of the CERN SPS hyperon experiment (CERN WA62). We have only been discussing states composed of the three lowest mass quarks. From Figure 1, it is clear that there is a much richer structure. Figure 44 depicts the structure of the three quark baryons when the c (charm) quark is also included.

There has been a continual upgrade in the number of detector planes, their spatial resolution, and the particle identification capabilities of this apparatus. Figure 45 shows a baryon mass spectrum[8,64] of a state they named A^+ and concluded to have a quark stucture of csu. In modern nomenclature (shown in Figure 44) this is the Ξ_c^+. Since the incident beam particle could be tagged, this production was shown to be initiated by a Σ^-. Shortly later they discovered[8,65] a css state they named the T°. In the notation of Figure 44 this is the Ω_c°.

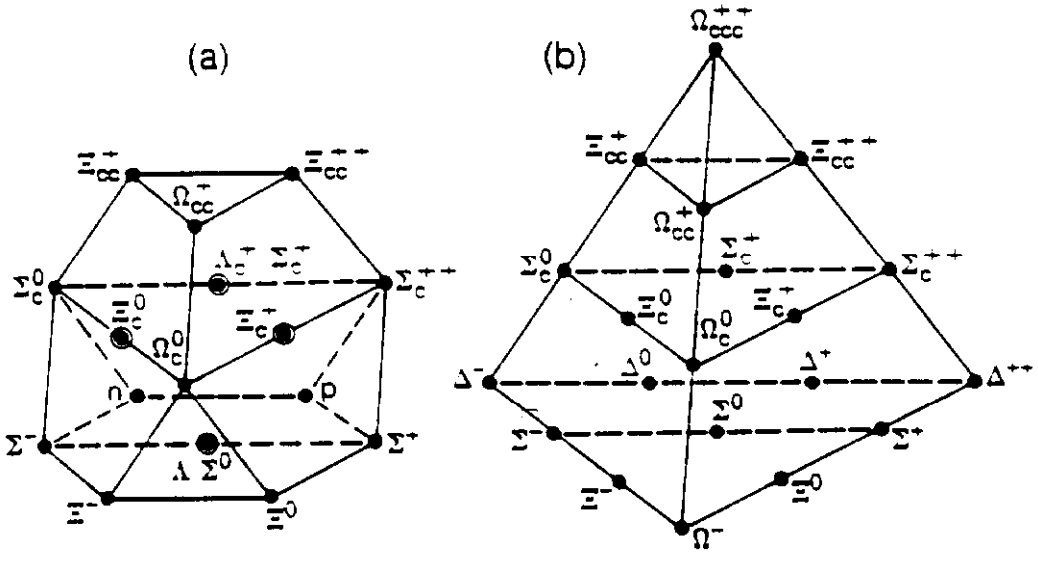

Figure 44. Three quark states of $1/2^+$ and $3/2^+$ which form two SU(4). These correspond to quantum numbers of C=0 to C=3.

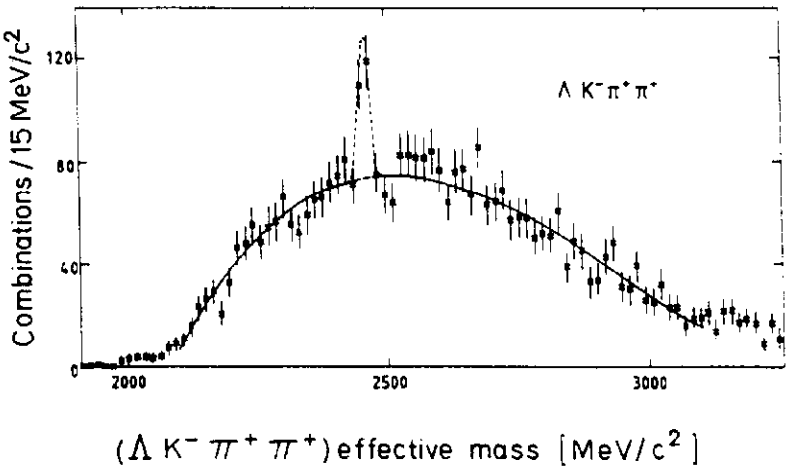

Figure 45. Evidence for a Ξ_c^+ (csu) state from the CERN hyperon experiment

These discoveries were not followed up by the CERN group because the space occupied by their beam was needed for other projects.

It is clear that a rich program of baryon spectroscopy is before us. It is one in which the advantage of an incident projectile which carries a strange quark has an advantage in producing a state with both charm (or perhaps even beauty) and strangeness. A new program is under way at CERN (WA89) and at Fermilab (E781) to continue in this direction.

References

1. Particle Data Group, *Phys. Lett.* **B239**, (1990) 1.
2. L. K. Gershwin, UCRL-19246, PhD Thesis, U. of California, Berkeley, 1969.
3. E. Segre, *Nuclei and Particles*, W. A. Benjamin, Inc. 1965.
4. F. T. Dao et al., *Phys. Rev. Lett.* **29** (1972) 1627.
5. J. Lach and L. Pondrom, *Ann. Rev. Nucl. Part. Sci.* **29** (1979) 203.
6. L. Pondrom, *Phys. Rep.* **122** (1985) 57.
7. J.M. Gaillard and G. Savage, *Ann. Rev. Nucl. Part. Sci.* **34** (1984) 351.
8. M. Bourquin and J. P. Repellin, *Phys. Reports* **114** (1984) 100.
9. T. R. Cardello et al., *Phys. Rev.* **32** (1985) 1.
10. J. Badier et al., *Phys. Lett.* **B39**, (1972) 414.
11. V. Hungerbuehler et al., *Nucl. Instr. and Methods* **115** (1974) 221.
12. V. Hungerbuehler et al., *Phys. Rev.* **D12** (1975) 1203.
13. S. F. Biagi et al., *Nucl Phys* **B186**, (1981) 1.
14. R. Majka et al., Phys. Rev. Lett **37** (1976) 413
15. C. Wang et al., *Phys. Rev.* **D10** (1974) 2051.
    Arik, E. et al., *Phys. Rev. Lett.* **38** (1977) 1000.
16. S. F. Biagi et al., *Z. Phys. C, Particles and Fields* **17** (1983) 113.
17. S. F. Biagi et al., *Z. Phys. C, Particles and Fields* **31** (1986) 33.

18. E. D. Commins & P. H. Bucksbaum, *Weak Interactions of Leptons and Quarks*, Cambridge University Press, 1983.
19. L. B. Okun, *Leptons and Quarks*, North Holland Publishing Co. 1982.
20. K. Heller et al., *Phys. Rev. Lett.* **51** (1983) 2025.
21. K. B. Luk et al., *Phys. Rev.* **D38** (1988) 19.
22. G. Bunce et al., *Phys. Rev. Lett.* **36** (1976) 1113.
23. P. M. Ho et al., *Phys. Rev. Lett.* **65** (1990) 1713.
24. K. Heller et al., *Phys. Rev. Lett.* **41** (1978) 607.
25. J. Franklin, *Phys. Rev.* **172** (1968) 1807.
26. S. A. Gourlay et al., *Phys. Rev. Lett.* **56** (1986) 2244.
27. G. Gustafson, *Proceedings of the 1982 Spin Conference* (BNL) 355.
Also see B. Anderson, *Nucl. Phys.* **A461** (1987) 513
28. T. A. DeGrand and H. Miettinen, *Rev.* **D23** (1981) 1227.
T. A. DeGrand, *Phys. Rev.* **D38** (1988) 403.
29. P. Kroll, *AIP Conf. Proc. 187, High Energy Spin Physics* (1989) 48.
30. M. Gell-Mann, *Synchrotron Laboratory, California Institute of Technology, Internal Report No. CTSL-20, 1961* (unpublished),
S. Okubo, Progr. *Theoret. Phys.* (Kyoto) **27**, (1962) 949.
31. V. E. Barnes et al., *Phys. Rev. Lett.* **12** (1964) 204.
32. M. Deutschmann et al., *Phys. Lett.* **73B** (1978) 96.
M. Baubillier et al., *Phys. Lett.* **78B** (1978) 342.
33. M. Bourquin et al., *Nucl. Phys.* **B241** (1984) 1.
34. K. B. Luk, Invited talk at the 9th International Symposium on High Energy Spin Physics, Bonn, Germany, Sept. 1990.
35. H. T. Diehl, III, Omega Minus Polarization and Magnetic Moment. PhD thesis, Rutgers University, 1990.
36. H. T. Diehl et al., Measurement of the Ω^- Magnetic Moment, Fermilab-Pub-91/165, submitted to *Phys. Rev. Lett.*
37. T. A. DeGrand et al., *Phys. Rev.* **D32** (1985) 2445.
38. Cohen, *Rev. Mod. Phys.* **69** (1987) 1121.
39. P. Winkler et al., *Phys. Rev.* **5A**, (1972) 83.
40. G. L. Greene et al., *Phys Rev.* **20D**, 2139 (1978).
41. B. L. Roberts, *Phys. Rev.* **17D**, (1978) 358.
Hu et al., *Nucl. Phys.* **A245**, (1975) 403.
42. D. W. Hertzog et al., *Phys. Rev.* **D37**, (1988) 1142.
43. G. Zapalac et al., *Phys Rev Lett.* **29**, (1986) 1526.
Y. Wah et al., *Phys. Rev. Lett.* **55**, (1985) 2551.
L. Deck et al., *Phys. Rev.* **D28**, (1983) 1.
44. H. Primakoff, *Phys. Rev.* **31**, (1951) 899.
Dreitlein and Primakoff, *Phys. Rev.* **125**, (1962) 1671.
45. L. C. Schachinger et al., *Phys Rev Lett.* **41**, (1978) 1348.
L. C. Schachinger, Ph.D. Thesis, Rutgers University, 1978 (unpublished).
46. Cox et al., *Phys Rev Lett.* **46**, (1981) 877.
47. C. Ankenbrandt et al., *Phys. Rev. Lett.* **51**, (1983) 863.

48. C. Wilkinson et al., *Phys. Rev. Lett.* **58**, (1987) 855.
49. G. Rameika et al., *Phys. Rev. Lett* **52**, (1984) 581.
50. L. H. Trost et al., *Phys. Rev.* **D40** (1989) 39.
51. Kinoshita et al., *Phys. Rev. Lett* **47**, (1981) 1573.
52. P. C. Petersen et al., *Phys. Rev. Lett* **57**, (1986) 949.
53. J. S. Foster et al., *Nucl. Phys.* **B318**, 301 (1989). See also Relativistic Channeling, Edited by R. Carrigan, Jr. and J. A. Ellison, Plenum Press, New York, 1987.
54. Hara, *Phys. Rev. Lett.*, **12** (1964) 378
55. Kogan and Shifman, *Sov. J. Nucl. Phys.* **38** (1983) 4
56. M. K. Gaillard, X. Q. Li, and S. Rudaz, *Phys. Letters* **158B**, 158(1985)
57. I. I. Balitsky, V. M. Brawn, A. V. Kolesnichenko, *Sov. J. Nucl. Phys.* **44**, 1028(1986)
58. D. Palle, Phys. Rev. **D36**, 2863(1987)
59. Y. I. Kogan and M. A. Shifman, *Sov. J. Nucl. Phys.* **38**, 628(1983)
60. F. J. Gilman and M. B. Wise, *Phys. Rev.* **D19** 976(1979)
61. C. Goldman and C. O. Escobar, *Phys. Rev.* **D40** 106(1989)
62. M. D. Scadron and M. Visinescu, *Phys. Rev.* **D28**, 1117(1983)
63. M. Foucher, *XXVIth Recontres de Moriond, Les Arcs, Savoie-France*, Fermilab-Conf-91/112, May 1991.
64. S. F. Biagi et al., *Phys. Lett.* **122B**, (1983) 455.
65. S. F. Biagi et al., *Z. Phys. C, Particles and Fields* **28** (1985) 175.